ACS APPLIED NANO MATERIALS

www.acsanm.org Article

Silver-Loaded Xerogel Nanostructures for Iodine Capture: A Comparison of Thiolated versus Unthiolated Sorbents

Brian J. Riley,* Saehwa Chong, José Marcial, Nabajit Lahiri, Mrinal K. Bera, Sungsik Lee, Tianpin Wu, Karen Kruska, and Josef Matyáš

Cite This: *ACS Appl. Nano Mater.* 2022, 5, 9478−9494 Read Online

ACCESS | Metrics & More | Article Recommendations | Supporting Information

ABSTRACT: This paper describes the development and provides comparisons of thiolated (−SH) and unthiolated Ag−Al−Si−O xerogels for iodine gas capture. These xerogels were produced from alkoxides and then heat-treated at 350 °C to provide mechanical strength for subsequent processing steps. Then, a portion of the xerogels was thiolated using (3-mercaptopropyl)trimethoxysilane. Next, thiolated and unthiolated batches were ion-exchanged in $AgNO_3$ solutions where Ag^+ replaced Na^+ in the gel network on a near 1:1 molar basis. Subsamples of the Ag-exchanged xerogels were subjected to a reduction step in H_2/Ar to convert Ag^+ to Ag^0 where the rest of the Ag-exchanged (Ag^+) were not reduced. X-ray diffraction, X-ray photoelectron spectroscopy, and transmission electron microscopy revealed nanoscale Ag^0 in the Ag^+ samples despite no active reduction where actively reduced samples had bimodal Ag^0 distribution of ∼2−3 nm hexagonal and ∼6−7 nm cubic crystallites. Synchrotron X-ray absorption spectroscopy was used to assess the oxidization states of Ag, S, and I within the different xerogel samples. The specific surface areas of the base xerogels decreased as subsequent treatments were performed on the as-made samples, albeit the decreases were smaller than aerogel equivalents of these samples from a previous study. All iodine-loaded Ag-based samples showed a mixture of β-AgI and γ-AgI. Comparisons of iodine-loading results with other Ag-based iodine sorbents show that the thiolated Ag^0-xerogels in this work have one of the highest iodine-loading capacities (q_e) reported to date in saturated conditions with the thiolated Ag^0-xerogel showing 522 mg iodine per g of the sorbent.

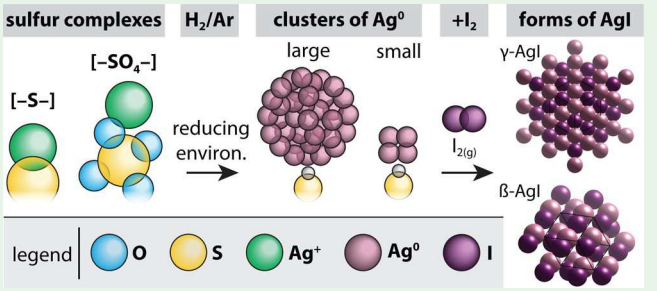

KEYWORDS: *iodine capture, xerogels, silver-based sorbents, X-ray absorption spectroscopy, X-ray photoelectron spectroscopy, thiolation*

1. INTRODUCTION

While iodine is an integral part of human metabolism and is often found in common foods, radioiodine is indistinguishable by the body, and the uptake by the thyroid can lead to cancer. The two most prevalent forms of radioiodine that are of interest include short-lived and highly active ^{131}I with a half-life ($t_{1/2}$) of 8.02 d and long-lived ^{129}I with a $t_{1/2}$ of 1.57×10^7 y. Several different types of radioiodine sorbents have been reported for capturing iodine as a gas in different forms [e.g., $I_{2(g)}$ and $CH_3I_{(g)}$] or as an ion from liquid effluents (e.g., I^- and IO_3^-).[1−5] The primary types of iodine capture systems include solid sorbents or liquid scrubber systems, often utilizing an aqueous hydroxide or molten hydroxide.[2,3,6] A wide range of solid sorbents have been reported that typically utilize active metal sites targeted to remove the iodine species from the environment through physisorption and/or chemisorption mechanisms. Some examples of solid sorbents include activated carbon;[7] metal-exchanged zeolites like Ag-mordenite (Ag-MOR or AgZ), Ag-faujasite (Ag-FAU or AgX and AgY), and Ag-Linde type A (AgA);[8−14] metal−organic frameworks;[15,16] metal-loaded aerogels or xerogels;[17,18] metal-impregnated ceramics;[19] and solid metal substrates.[20,21] The current work will focus primarily on chemisorption-based iodine capture.

For solid sorbents, the sorbent typically comprises a porous scaffold into (or onto) which metal getters are added. For zeolites, the getter metals are often installed through an ion exchange process by replacing some of the cations with the getter ions of choice. Additional approaches can be implemented for installing getters, such as the utilization of tethers to bind the getter metal indirectly. This is accomplished by functionalizing the gel surfaces with an intermediate "tether" layer whereby the getter bonds to this layer instead of directly to the scaffold. An example of this type of tether approach is to use thiol groups that can be installed through surface treatment with (3-mercaptopropyl)trimethoxysilane (abbreviated here as 3-MPTMS),[22,23] which was utilized in the current study.

Received: April 21, 2022
Accepted: May 27, 2022
Published: June 16, 2022

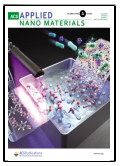

https://doi.org/10.1021/acsanm.2c01741
ACS Appl. Nano Mater. 2022, 5, 9478−9494

The selection of the getter metal is of particular concern because it will dictate the iodine-loading capacity as well as several other variables described below. One of the more commonly studied getter metals is Ag but others include Bi,[24−26] Cd,[27] Cu,[20,28] Pb,[27] Sn,[28] and Zn.[27] Aspects worth considering when choosing the active metal getter include (1) the thermodynamics of metal-iodide formation versus metal-oxide formation, (2) the kinetics (capture rate) of the getter−iodine reaction, (3) the cost of the metal, (4) chemical hazards of the metal, (5) the process(es) required to install the metal on the surface of a sorbent, (6) the oxidation state of the getter, (7) the stability (e.g., chemical, thermal, and mechanical) of the scaffold framework holding the getter, and (8) the disposal pathways for the final iodine-containing product (i.e., the chemical durability for disposal within a repository environment).

For the first aspect, the thermodynamic properties are critical because, if the capture process is performed in an oxygenated environment, the spontaneity to form the metal-iodide has to be higher than that of the metal-oxide or the metal will oxidize (and likely convert to a metal oxide) before it can react with iodine. A recent study based on thermodynamic calculations of Gibbs free energies of formation (ΔG_f°) using HSC Chemistry (Reaction Module, v9.9.0.1) revealed that very few metals fit this requirement and only under specific temperature ranges where Ag showed the highest preference for metal-iodide formation over the metal oxide.[18] When forming some metal compounds, the tendency to form the oxide over the iodide (i.e., ΔG_f°,o < ΔG_f°,i) is preferred at elevated temperatures for Pb^{2+} ($T \geq 125$ °C), Pt^{2+} ($T \geq 175$ °C), and Pt^{4+} ($T \geq 50$ °C), while the opposite is true for metals like Tl^{+} ($T \leq 400$ °C). While these predictive tools are helpful, in practice, some metal-iodide reactions are more complicated than this simplistic approach and will likely require a delicate understanding of potential intermediate reactions between the starting and end points within the relevant temperature ranges and expected real-world environment including potential interfering species (e.g., other halide gases).

Second, the kinetics aspect is also important here because different metals can show different metal-iodine reaction rates. The kinetics of these reaction are also likely affected by the oxidation state and form of the getter (e.g., oxides vs oxyhydroxides vs metals), the size of the installed getters (e.g., nanocrystals vs microcrystals), and the accessibility of the getter [e.g., low vs high specific surface area (SSA) scaffolds].

Third is the cost of the metal-based precursor selected as this can vary extensively. While Ag is a precious metal, it can be less expensive than some other non-precious metals based on the form factor required for installation onto or into the scaffold [e.g., $AgNO_3$ vs Sn(IV) acetate]. If a tether is required to install the getter metal, this can add extra steps and costs. Some thought has also been given to the recovery of the Ag following iodine capture such as the reaction of AgI with Na_2S to form Ag_2S and NaI, as shown in eq 1,[29] the latter of which could be incorporated into a different waste form such as iodosodalite [i.e., $Na_8(AlSiO_4)_6I_2$][30,31] or iodoapatite [e.g., $Pb_{10}(VO_4)_6I_2$][29] starting from NaI. However, several other getter metals are available that could be less expensive such as Cu and Bi, albeit with different capture performances than Ag.[18,32]

$$2AgI_{(s)} + Na_2S_{(aq)} \rightarrow 2NaI_{(aq)} + Ag_2S_{(s)} \quad (1)$$

Fourth includes an assessment of safety and health hazards introduced by the getter metal of choice, which need to be taken into consideration. For instance, while Ag, Cd, Hg, and Pb might be effective iodine sorbents, they are all regulated by the US Environmental Protection Agency under the Resource Conservation and Recovery Act (RCRA) as toxic elements,[33] which might complicate disposal in a repository. Also, adding the getter metal into the sorbent as a nanoparticle might improve the capture performance but introduces nanomaterial hazards. These need to be taken into account when considering materials handling and disposal restrictions.

Fifth, while a getter metal might be very effective at capturing iodine species, and the most effective form is typically in a very small form factor (e.g., metal crystallites or ionic clusters nanometers in size), installing these into cages for zeolites or onto porous scaffolds can be difficult. Also, if the getter metal is installed in the ionic form, it can be actively reduced in some cases to exemplify the functionality of the sorbent further. In a recent study,[32] solid metal wires were used to capture iodine vapors in a saturated $I_{2(g)}$ environment, and some of the metals showed complete reaction over a 24 h period, suggesting that perhaps the nanoscale sized getter form factor is not required in certain applications for effective iodine capture.

Sixth, it is unclear whether or not the getter needs to be in the metallic state or if it can be at least partially oxidized prior to the reaction. The redox state optimization is likely inconsistent for different getter metals. It is also clear that both oxidized Ag (Ag^+) and metallic Ag (Ag^0) function as $I_{2(g)}$ getters when exposed to saturated environments.[23] The data presented in this paper show the similarities in samples made under like processes where, after Ag-exchanging the gels, batches were left in the oxidized Ag^+ state, while separate batches were actively reduced to Ag^0 and both perform well in iodine capture experiments. However, this could change depending on the selected getter metal.

The seventh point of interest includes the difference between the stabilities (e.g., acid resistance) of various silica and aluminosilicate substrates in representative off-gas environments pertaining to reprocessing of used nuclear fuel or remediation after nuclear accidents. These environments have moderate temperatures (i.e., $T > 100$ °C) and can contain oxidizing species (e.g., NO_x). Matyáš et al. demonstrated that thiolated Ag^0-functionalized silica aerogels can withstand oxidation and undergo far less aging-related effects in these environments than sorbents like Ag-MOR and this is due, at least in part, to the thiol groups helping prevent oxidation of the Ag^0 to Ag^+ during iodine-loading experiments.[17,34] The higher silica content is also part of the justification for why zeolites like Ag-MOR (i.e., Si/Al = 5) perform better and are more durable in these oxidizing environments than lower-silica zeolites like Ag-FAU (Si/Al ∼ 1.0−1.5 for AgX and ∼ 1.5−3.0 for AgY).[10,35−38] These types of parameters are important when comparing sorbents that might perform similarly in some testing conditions but could be very different in other conditions (e.g., higher oxidizing environments with higher temperatures).[39] The mechanical stability and integrity of the base sorbent are also paramount as off-gas sorbents can be subjected to large pressures in high-flow systems, and it is necessary for the sorbent to remain intact (i.e., not friable) so sorbent particles do not transport downstream in the collection system. Upon a metal-iodine reaction, the volume of the initial getter form is expanded due to the added iodine mass (e.g., Ag and Cu metal wires[39]). This is often observed as the formation of crystalline metal-iodide complexes (e.g., AgI) and can even result in the amorphization of the scaffold crystal structure (e.g., Ag-FAU).[39] If these metal-iodide crystals grow too large for the scaffold to

https://doi.org/10.1021/acsanm.2c01741
ACS Appl. Nano Mater. 2022, 5, 9478−9494

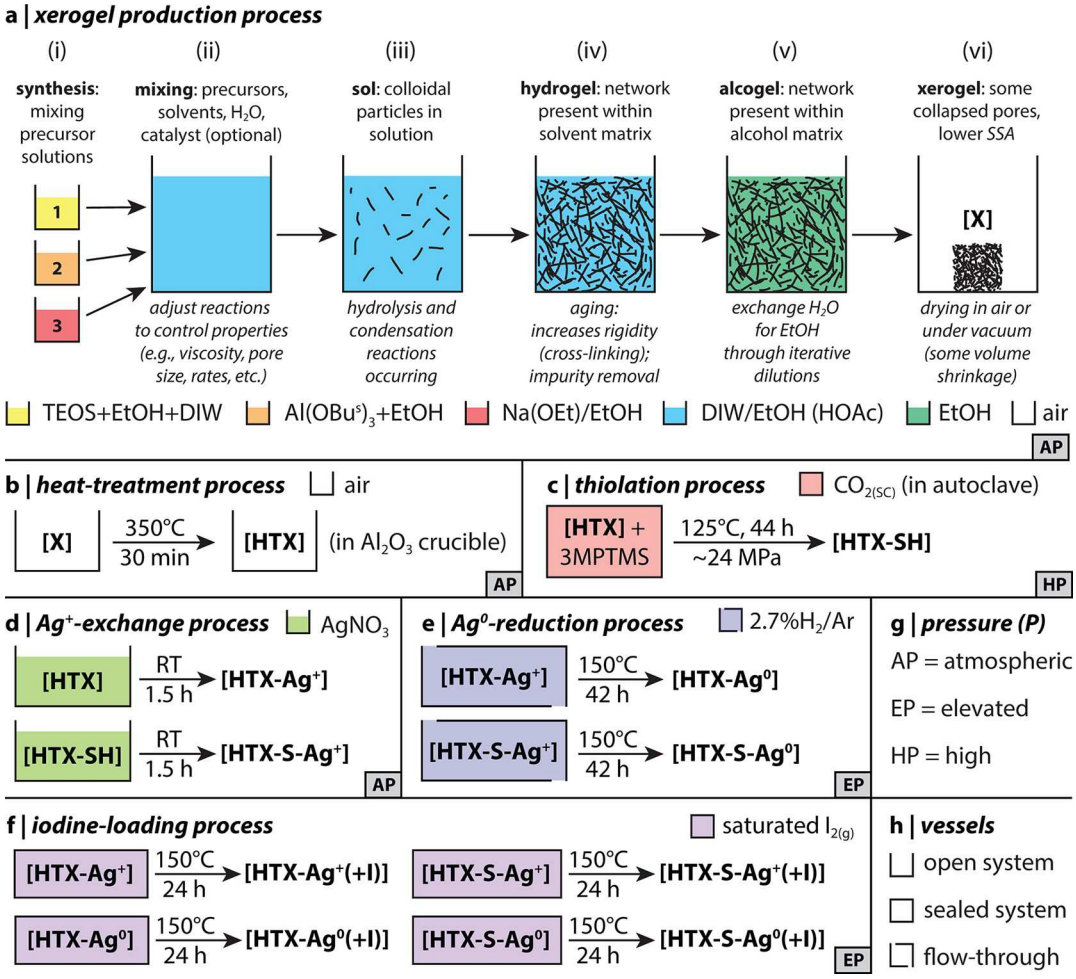

Figure 1. Summary of sample preparation processes including (a) making xerogels including (i) mixing precursors, (ii) mixing precursor solutions together including the catalyst, (iii) creating the sol, (iv) making the hydrogel, (v) making the alcogel, and (vi) making the xerogel; (b) heat-treatment (HT) process; (c) thiolation process [in supercritical CO_2 or $CO_{2(SC)}$]; (d) Ag^+ exchange process; (e) Ag^0 reduction process; (f) iodine-loading process; (g) pressure designations (AP = atmospheric pressure, EP = elevated pressure, and HP = high pressure) for a given procedure; and (h) vessel types designated in the graphics (i.e., open or closed). RT denotes room temperature; other definitions are provided in the text. Reprinted (in part) with permission from Riley et al.[23] Copyright 2017 American Chemical Society.

hold them effectively or the scaffold becomes friable due to the volume expansion upon iodine capture, it is possible that the process of iodine loading and scaffold amorphization could facilitate downstream release of the metal-iodide particles.

The last point is the chemical durability of the final metal iodide form in the sorbent after capture.[40] While several metal iodides are found in nature with base metals often existing at different oxidation states, only a select few have low leach rates, especially when excluding metals like Hg due to high inherent toxicities. This is important when considering the fate of the material after iodine loading, which includes the final disposition pathway in a geologic repository.[41] Of the existing metal iodides, CuI ($K_{sp} = 1.27 \times 10^{-12}$), AgI ($K_{sp} = 8.52 \times 10^{-17}$), and Bi ($K_{sp} = 7.71 \times 10^{-19}$) have some of the lower solubility product constants and should lead to chemically durable final forms.[42]

The current study was aimed at evaluating thiolated versus unthiolated Ag-based xerogel sorbents that utilize a chemisorption-based $I_{2(g)}$ capture mechanism to create AgI crystals within the sorbent matrix. Several parameters were investigated including the Ag^+/Ag^0 redox state of the base materials, the oxidation state of S (i.e., thiol vs sulfate) in thiolated samples, the SSAs of samples after various stages of sample treatment, as well as the microstructure, nanostructure, and crystalline nature of the materials before and after iodine loading. In all cases, all Ag-loaded sorbents performed effectively at capturing large amounts of $I_{2(g)}$, but some sample preparation variables seem to be more essential at maximizing capture than other variables. The main goal of this study was to provide more information to help advance scientific research regarding the performance impacts of various sample treatments on $I_{2(g)}$ capture in saturated environments.

2. MATERIALS AND METHODS

2.1. Sample Preparations. A summary of the sample preparation process is presented in Figure 1. The major categories of preparation include the xerogel production process (Figure 1a), the heat-treatment (HT) process (Figure 1b), the thiolation process (Figure 1c), the Ag^+-exchange process (Figure 1d), the Ag^0-reduction process (Figure 1e), and the iodine-loading process (Figure 1f). More details for each of these processes are provided in the subsections below.

2.1.1. Xerogel Production Process. A batch of $NaAlSiO_4$ gels with an approximate target solid mass of 5 g was made using sodium ethoxide (NaOEt; $NaOC_2H_5$, 21% by volume in ethanol or EtOH; Sigma-Aldrich) along with ethanol (EtOH) at a 6:1 (V V^{-1}) mixture with aluminum tri-*sec*-butoxide [$Al(OBu^s)_3$; 97%, Sigma-Aldrich] using pre-hydrolysis and an acetic acid (HOAc; glacial, Sigma-Aldrich) catalyst.

https://doi.org/10.1021/acsanm.2c01741
ACS Appl. Nano Mater. 2022, 5, 9478−9494

Here, 7.94 mL of EtOH, 0.634 mL of deionized water (DIW; 18.2 MΩ cm), 7.94 mL of tetraethyl orthosilicate (TEOS; 99%, Sigma-Aldrich), and 0.101 mL of HOAc were added to a Teflon beaker and mixed for 6 h (i.e., 1:1 V V^{-1} of TEOS/EtOH; 1:1 TEOS/DIW, by mole; 1:0.05 TEOS/HOAc, by mole), at which point it was moved to a nitrogen glovebox (M-Braun, Germany), and mixing was resumed. Then, 55.46 mL of EtOH (200 proof, Decon Labs, Inc.) was added to this solution immediately followed by 9.24 mL of $Al(OBu^s)_3$; the solution turned cloudy white when the $Al(OBu^s)_3$ was added. After mixing overnight (~19 h), 13.14 mL of NaOEt was slowly added dropwise to this mixture over the course of 10 min and, about halfway through this addition, the solution appeared yellow in color. Then, 4 h later, the solution was taken out of the glovebox, and 2.536 mL of DIW was added. Finally, after 30 min of stirring, the mixture was cast into 4 mL polypropylene vials (Wheaton Omni-Vial), capped with tightly fitting lids and left to undergo gelation (i.e., Figure 1a-i,ii). The gelation time (t_{gel}) was determined by visual observations of the rigidity of the mixture (i.e., Figure 1a-iii,iv). Following gelation, the gels were removed from their vials, cut into smaller pieces of ~2−8 mm with a stainless-steel razor, and placed into a 50% solution of EtOH in DIW (V V^{-1}). The 50% EtOH solution was replaced 10 times in 17 days while the gels were aging. This process helps draw out the reaction byproducts and helps strengthen the gel network by providing additional water that can aid in completing the hydrolysis process in the hydrogel state (i.e., Figure 1a-iv). Following aging, the gels were solvent exchanged in pure EtOH 10 times to remove water in the pore structure and replace it with EtOH (alcogel stage; Figure 1a-v). To create xerogels (see Figure 1a-vi), EtOH-saturated alcogels were removed from the EtOH solution, placed into pre-tared Nalgene bottles, and placed into a glass vacuum desiccator. Here, the EtOH solvent matrix in the alcogels was evaporated under vacuum at room temperature for approximately 2 weeks until no more mass loss was observed.

2.1.2. Heat-Treatment Process on Xerogels. A portion (2.0205 g) of the as-made xerogel (X) was heat-treated in an alumina crucible in a Thermolyne box furnace for 30 min at 350 °C. The crucible containing the sample was inserted into the furnace at this temperature and removed after 30 min, so it was allowed to quickly heat but also air cool to room temperature afterward. The final mass of xerogel after HT was 1.7346 g (14.2 mass % decrease). After this process, the sample was placed into a separate 125 mL Nalgene container and stored at room temperature in a vacuum desiccator.

2.1.3. Thiolation Process. For the thiolation process, 0.8696 g of heat-treated xerogel (HTX) was poured into a 10 mL pressure vessel (Thar Instruments Inc.), 2 mL of 3-MPTMS [$HS(CH_2)_3Si(OCH_3)_3$, 95%, Sigma-Aldrich, St. Louis, MO] was added with a syringe, and the vessel was sealed and heated to 150 °C with a silicone heat tape. Then, supercritical CO_2 (~24 MPa or ~3500 PSI) was charged into the vessel, using a syringe pump connected to the CO_2 bottle with a syphon draw tube, after the temperature of the vessel reached 125 °C. The sample was soaked under these conditions for 44 h before removing any residual (unreacted) silane by flushing the system with 150 mL of supercritical CO_2. This was carried out twice with a 10 min soak between each flushing. To determine the mass gain, the sample was removed and weighed on a 4-digit balance (1.1277 g). The sample gained 29.7 mass %, indicating a good coverage of the xerogel surface. The product resulting from this procedure was a thiolated HTX material denoted as HTX-SH.

2.1.4. Ag^+-Exchanging Gels. Two separate experiments were run for the Ag^+-exchanging process, including one for HTX and one for HTX-SH. Here, two 350 mL solutions were prepared by dissolving ~10.3 g of $AgNO_3$ (≥99%, Sigma-Aldrich) in a 5:1 V V^{-1} solution of DIW/EtOH (292:58 mL) and stirred for 1 h on a magnetic stir plate. Approximately 0.70 g each of the HTX and HTX-SH gels were separately added into the different solutions and stirred for 1.5 h. The ratio of gel mass to moles of $AgNO_3$ ($m_s M_{Ag}^{-1}$) in these solutions was ~11.5 g mol^{-1}. After soaking, the gels were removed and placed in pre-tared 20 mL scintillation vials, and then these vials (with loosened caps) were placed in a vacuum desiccator for drying. The extent of Ag exchange into the base materials was evaluated using energy-dispersive X-ray spectroscopy (EDS) on powdered forms of the materials (discussed in a later section).

2.1.5. Ag^0-Reduction Process. About 0.5 g each of HTX-Ag^+ and HTX-S-Ag^+ were utilized in the silver reduction test. The samples were loaded into separate 15 mL columns, heat-treated at 150 °C for 42 h under 10 mL/min of flowing 2.7% H_2/Ar; more information on this process can be found in our previous work for treating aerogels.[23] Each sample was weighed before and after for mass changes, and both samples lost some mass during the process. Both samples were dark black in color following the reduction process, confirming reduction of silver ions to metal.

2.1.6. Iodine Capture Process. To assess the iodine loading in the different samples, granules of each material were placed into 4 mL glass vials (Qorpak GLC-00980), which were in turn placed into a 1 L perfluoroalkoxy (PFA) vessel (100-1000-01; Savillex; Eden Prairie, MN) along with a 20 mL glass scintillation vial containing 0.8341 g of solid iodine pieces (m_I, ≥ 99.9%, Sigma-Aldrich); the ratio of m_I to total sample mass [i.e., $m_I/\Sigma_{j=1}^{n}(m_s)_j$; where j denotes different samples] was 1.0228. Masses were obtained using the ME204E analytical balance. An additional empty vial (the blank) was added to assess the iodine capture on the vial itself, which was taken into account in subsequent calculations. Then, the Savillex vessel was placed into an oven (3511FSQ, Isotemp, Fisher Scientific; Hampton, NH) at 150 °C (±4 °C) for 24 h. Following this soak, the vials were carefully removed from the apparatus and placed directly into the same oven at 150 °C for 1 h without the iodine present so that any physisorbed iodine could be desorbed. Sample names after iodine loading are denoted with "+I" suffixes.

Following the iodine-loading experiments, eqs 2−4 were used to evaluate the gravimetric iodine capacities based on the mass uptake where m_s is the starting mass of the sample, m_{s+I} is the final mass following iodine capture, m_I is the mass of iodine captured by the sample by mass difference from m_s [eq 2], $m\%_I$ is the mass % of iodine in the final sample [eq 3], and "g g^{-1}" is the term denoting the mass of iodine captured per starting mass of the sorbent (gravimetric iodine loading) [eq 4]. Alternatively, eq 4 can be written in terms of mg g^{-1}, which is often referred to as q_e and is essentially $1000 \times [m_I/m_s\,(\mathrm{g\,g^{-1}})]$. Finally, the Ag-utilization (AgU) was calculated as the ratio of I to Ag in the iodine-loaded gels, as shown in eq 5, using data collected from EDS analyses in atomic % with built-in standards in the Bruker ESPRIT software. When AgU > 1, some physisorbed iodine may remain within the sample or iodine is binding to a different location within the sorbent compared to the Ag getter including directly to the aerogel surface.

$$m_I = m_{s+I} - m_s \tag{2}$$

$$m\%_I = 100 \times (m_I/m_{s+I}) \tag{3}$$

$$\text{I-loading} = m_I/m_s(\text{or g g}^{-1}) \tag{4}$$

$$\text{AgU} = 100 \times [\text{I}]/[\text{Ag}]\ (\text{at \%/at\%}) \tag{5}$$

2.2. Sample Pictures and Dimensional Analyses. Pictures were taken of the samples using a Canon Rebel T1i digital camera using Canon OES software with a circular polarizer filter. For getting scale bars on the images, each image was collected at the same magnification (zoom), and a ruler was included in each picture (not shown) so that a scalebar could be added to the final image composite using Adobe Photoshop (v22.5.0). Measurements were made on various samples during the hydrogel stage (aging in 50/50 DIW/EtOH solution), alcogel stage (100% EtOH solution), xerogel stage (after drying), and HTX (after HT). Pictures for these measurements were captured with rulers in the images (liquid-emersed samples) or using a set of digital calipers (±0.01 mm). Values reported are average values for all but the alcogel sample from multiple measurements. Areas (A) were calculated using the measured diameters (d) [i.e., $A = \pi\cdot(0.5\cdot d)^2$], and volumes ($V$) were also calculated from the diameter values assuming equal shrinkage in all directions [i.e., $V = 4/3\cdot\pi\cdot(0.5\cdot d)^3$]. Of course, these measurements were only used as estimates because the assumption of regular shrinkage in all dimensions was not expected in all cases.

https://doi.org/10.1021/acsanm.2c01741
ACS Appl. Nano Mater. 2022, 5, 9478−9494

2.3. X-ray Absorption Spectroscopy. X-ray absorption near edge structure (XANES) spectroscopy was performed near the Ag K-edge (25.514 keV), I L_3-edge (4.557 keV), and S K-edge (2.4695 keV) at the Advanced Photon Source (APS) at Argonne National Laboratory. The Ag K-edge XANES analyses were performed utilizing beamline 12-BM-B operated in the fluorescence mode using a Si(311) monochromator and calibrated using Ag foil. The step sizes for Ag K-edge measurements were 5.0 eV (for the energy range of 25.314−25.499 keV), 0.6 eV (for 25.499−25.544 keV), and 0.05 $Å^{-1}$ (for 25.545−26.369 keV).

The I L_3-edge XANES analyses were performed utilizing beamline 12-BM-B and 9-BM-B operated in the fluorescence mode using a Si(111) monochromator and calibrated using AgI powder. The step sizes for I L_3-edge measurements were 5.0 eV (for the energy range of 4.410−4.547 keV), 0.4 eV (for 4.547−4.577 keV), and 0.05 $Å^{-1}$ (for 4.577−4.800 keV).

The S K-edge XANES analyses were performed utilizing beamline 9-BM-B operated in the fluorescence mode using a Si(111) monochromator and calibrated using sodium thiosulfate ($Na_2S_2O_3$) powder. The step size for S K-edge measurements were 2.0 eV (for the energy range of 2.319−2.449 keV), 0.15 eV (for 2.449−2.509 keV), and 0.05 $Å^{-1}$ (for 2.509−3.015 keV).

For Ag K-edge and I L_3-edge measurements, approximately 5−10 mg of sample powders and standards were separately mixed with ∼20 mg of BN binder (Alfa Aesar, 99.5%), pressed into 7 mm diameter pellets at 70 MPa using a uniaxial press, and then cut to fit the sample holders. Linear combination fittings of Ag K-edge XANES spectra were performed to estimate the Ag speciations in the samples and the redox ratio of Ag^+/Ag^0. This approach assumed that each sample was a linear combination of measured spectra (s_i) from Ag^0 (Ag metal) and Ag^+ species [i.e., Ag_2O (Noah, 99.5%), Ag-MOR (provided by Abney et al.[43]), and AgI (Sigma-Aldrich, 99.999%) after iodine sorption] with these four species summing to 1, as shown in eq 6, where r_i is the mole fraction of species "i" within the sample. The redox ratios for the four samples were fit to data using a least-squares approach.

$$\sum_{i=1}^{n} r_i s_i = r_1[Ag^0] + r_2[Ag_2O] + r_3[AgMOR] + r_4[AgI] = 1 \quad (6)$$

To aid the interpretation of S K-edge measurements, sample spectra were compared to the spectra of elemental S (ASARCO, 99.999%), Ag_2S (Sigma-Aldrich, 99.9%), Na_2SO_3 (Allied, 98%), and $CaSO_4*12H_2O$ (Fisher Scientific, 98%) standards. To aid the interpretation of I L_3-edge measurements, sample spectra were compared to the spectra of elemental I, NaI, AgI (Sigma-Aldrich, 99.999%), $NaIO_3$, and $NaIO_4$ (Johnson Matthey Co., 98%) standards where the spectra of elemental I, NaI, and $NaIO_3$ were collected and provided by Cicconi et al.[44]

2.4. Small-Angle X-ray Scattering. Small-angle X-ray scattering (SAXS) was performed at the 15-ID-D station of NSF's ChemMatCARS, Sector 15 of the APS. The list of samples analyzed included HTX, HTX-Ag^+, HTX-Ag^0, HTX-Ag^+(+I), and HTX-Ag^0(+I). Measurements were performed in the Q range of 0.006 and 0.3 $Å^{-1}$. The powdered samples were sandwiched between two Kapton films within a nylon washer that was 1 mm thick.

2.5. X-ray Photoelectron Spectroscopy. X-ray photoelectron spectroscopy (XPS) was performed on a Kratos AXIS Ultra DLD system using a monochromatic Al K_α source ($h\nu$ = 1486.7 eV) operating at 150 W. The samples analyzed were the four different Ag-containing sorbents without iodine (i.e., HTX-Ag^+, HTX-Ag^0, HTX-S-Ag^+, and HTX-S-Ag^0). Each sample was finely ground and pressed onto double-sided conductive carbon tabs (Ted-Pella Inc.) attached to a silicon substrate for analysis. During analysis, the chamber pressure was maintained at or below 2×10^{-9} Torr, and any surface changing was minimized using a low-energy electron flood gun. The binding energy (BE) scale of the instrument was calibrated to give a BE of 84.0 ± 0.1 eV for the Au $4f_{7/2}$ feature of metallic gold and 932.6 ± 0.1 eV for Cu $2p_{3/2}$ of metallic copper. Survey spectra were acquired at a pass energy (PE) of 160 eV with a step size of 1 eV, while high-resolution scans were performed at a PE of 40 eV with a step size of 0.1 eV. A sputter-cleaned gold foil yielded a full width at half-maximum (FWHM) of 1.9 eV at a PE of 160 eV and FWHM of 0.8 eV at PE of 40 eV.

The acquired data were processed using CasaXPS software and were charge referenced to adventitious C 1s (C−C/C−H component) at 285 eV. Data fitting was performed using product Gaussian−Lorentzian type curves with an Iterated Shirley background approximation. The Ag 3d and S 2p features were fit using a sufficient number of spin−orbit split doublets of equal FWHM. The separation between the Ad $3d_{5/2}$ and Ag $3d_{3/2}$ spin−orbit split components was constrained to 6 eV, whereas the area of the Ag $3d_{3/2}$ component was set to 0.67× that of Ag $3d_{5/2}$. For the S 2p feature, the separation between the doublets was constrained at 1.18 eV, whereas the area of the S $2p_{1/2}$ component was set to 0.5× that of the S $2p_{3/2}$ component. The only allowed degrees of freedom in both cases were the intensities and BEs of the peaks. A modified Auger parameter (MAP),[45] which is given in eq 7, was used to provide a qualitative understanding of the chemical speciation of Ag where KE is the kinetic energy. The Ag MNN Auger features in the XPS spectra exhibit two distinct regions, namely, $M_5N_{45}N_{45}$ and $M_4N_{45}N_{45}$. For the calculations in this paper, the higher BE feature was used, which is $M_5N_{45}N_{45}$. Generally, Ag^0 is known to present a higher MAP value compared to oxidized Ag species.[45]

$$\text{MAP} = \text{KE}(M_5N_{45}N_{45}) + \text{BE}(\text{Ag } 3d_{5/2}) \quad (7)$$

2.6. X-ray Diffraction. Powder X-ray diffraction (P-XRD) was performed by grinding samples in an agate mortar and pestle and adding these ground powders onto a 25 mm zero-background silicon holder by first suspending in isopropanol, dropping onto the holder, and allowing the isopropanol to dry prior to analysis. This process resulted in better adherence of the sample on the holder and did not appear to affect the sample diffraction based on previous experience with similar gels. In the event, the isopropanol addition affects the pore structure of the gels during drying; the subsample portions used for P-XRD analyses were not used in other characterization techniques (e.g., SSA, pore size measurements, and electron microscopies). Samples were then analyzed with a D8 Advance (Bruker AXS Inc.; Madison, WI) diffractometer with Cu K_α emission. The instrument was equipped with a LynxEye position-sensitive detector with a collection window of 3° 2θ. Typical scan parameters were 5−70° 2θ with a step of 0.019° 2θ and a 0.5−2 s dwell at each step, but the dwell times were increased as needed to get better signal-to-noise values for low-signal samples. Bruker AXS DIFFRAC^{plus} EVA (v4.1) and TOPAS (v5) software programs were used to identify and quantify the crystalline phases, respectively. Whole pattern fitting was carried out according to the fundamental parameter approach.[46] In some cases, the R_{wp} values are provided, which is a weighted fitness metric for the statistical precision of the data set.[47]

2.7. Specific Surface Area and Pore Size Distribution. The SSAs, pore volumes (V_p), and pore sizes (s_p) were measured with nitrogen [$N_{2(g)}$] adsorption and desorption isotherms collected with a Quadrasorb EVO/SI (Quantachrome Instruments, Anton Paar). Samples were broken into 1−3 mm sized pieces to fit into pre-tared borosilicate type-C long cells with a 6 mm sample chamber bulb (part number 193621, Quantachrome Instruments) or type-B 9 mm long cells without bulb (part number 193652, Quantachrome Instruments). Sample masses ($m_{s,BET}$) were collected on the analytical balance (see Table S3, Supporting Information). The samples were degassed under vacuum at 25 °C for 24 h before the adsorption measurements. For each sample, nitrogen adsorption and desorption data were collected at 77.3 K with 54 measurements over a total run time of 15−28 h. The surface area was determined using the five point Brunauer−Emmett−Teller (BET) method.[48] The Barrett−Joyner−Halenda method was used for the pore size distribution calculations.[49]

2.8. Scanning Electron Microscopy and Energy-Dispersive X-ray Spectroscopy. Scanning electron microscopy (SEM) was performed on the specimens using a JSM-7001F field-emission gun microscope (JEOL USA, Inc.; Peabody, MA). For SEM analysis, samples were adhered to the double-stick carbon tape and sputter-coated with 2.5 nm of iridium metal to create a conductive coating using an EMS 150T ES sputter coater (Quorum Technologies Ltd., United Kingdom). The EDS was performed on the same powder mounts with a

https://doi.org/10.1021/acsanm.2c01741
ACS Appl. Nano Mater. 2022, 5, 9478−9494

Bruker xFlash 6|60 (Bruker AXS Inc.; Madison, WI) using ESPRIT (v2.0). The conditions used for data collection were 15 kV and ~50−80 k counts per second. For EDS analysis, a minimum of five locations were evaluated for each sample, including locations on separately prepared specimens, so that compositional averages and standard deviations could be calculated.

2.9. Scanning Transmission Electron Microscopy and Transmission Electron Microscopy. Samples were prepared for transmission electron microscopy (TEM) and scanning TEM (STEM) by crushing them between two glass slides. A standard lacy carbon TEM grid was guided across the resulting fine powder to collect particles suitable for analysis. TEM analysis was carried out in a JEOL ARM200CF equipped with a Centurio EDS detector. All TEM images were collected at bright-field conditions. Then, EDS mapping was carried out in the STEM mode. The HTX samples that did not contain Ag were prone to beam damage under prolonged exposure leading to drift during TEM imaging and EDS analysis that manifested in blurry micrographs despite limited acquisition times.

2.10. Helium Pycnometry and Skeletal Densities. Skeletal densities (ρ) of the samples were measured using a helium pycnometer (Micromeritics AccuPyc II 1340). Sample masses were weighed on the Mettler ME204E balance and inputted into the AccuPyc II software. Then, 10 volume measurements of each sample were performed with the pycnometer. The densities of each sample were calculated using the average volume and inputted mass for that sample.

3. RESULTS

3.1. Sample Appearances and Measurements (before Iodine). The sample appearances for the base materials are shown in Figure 2. The as-made xerogel (i.e., X in Figure 2a) and HTX (in Figure 2b) did not appear any different visually, and both samples were bright white in color. The thiolated HTX sample (i.e., HTX-SH in Figure 2c) was less bright white in color with a pinkish hue. The Ag^+-exchanged HTX-SH sample (i.e., HTX-S-Ag^+ in Figure 2d) was light brown in color, the Ag^+-exchanged HTX sample (i.e., HTX-Ag^+ in Figure 2f) was dark brown, and both Ag^0-reduced versions of these (i.e., HTX-S-Ag^0 in Figure 2e and HTX-Ag^0 in Figure 2g) were dark black in color. Size reductions were observed between the various initial stages including hydrogel > alcogel > xerogel > HTX, which are documented in Figure S12 (Supporting Information). The largest observed decrease within this sample set was during the alcogel → xerogel stage. During the silver reduction process, HTX-Ag^+ lost ~4.5 mass % (to create HTX-Ag^0) and HTX-S-Ag^+ lost ~8.4 mass % (to create HTX-S-Ag^0), indicating that they were not completely dry after the silver impregnation step to create these precursors. This could also explain some fine particles generated during the reduction process.

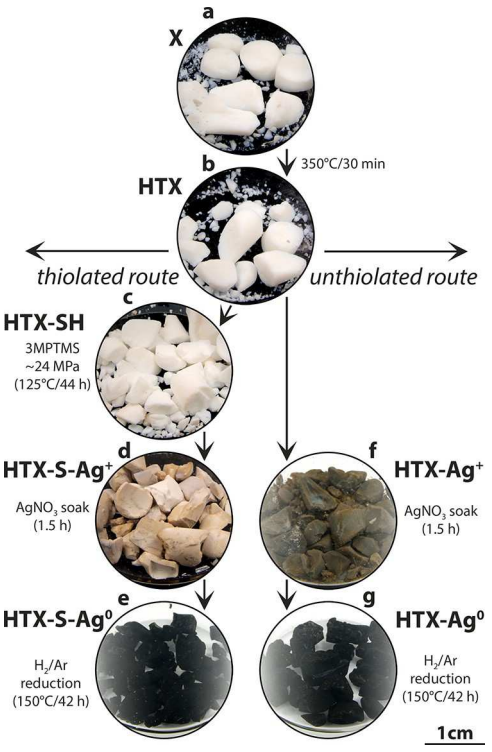

Figure 2. Pictures of the samples at various stages in the synthesis process including the (a) as-made xerogels (X), (b) HTXs, (c) thiolated HTX (HTX-SH), (d) Ag^+-loaded HTX-S (HTX-S-Ag^+), (e) Ag^0-loaded HTX-S (HTX-S-Ag^0), (f) Ag^+-loaded HTX (HTX-Ag^+), and (g) Ag^0-loaded HTX (HTX-Ag^0). Following thiolation, −SH tethers are installed on the gel surface and subsequent Ag processes remove H, and thus, the nomenclature changes for those samples. Samples were in glass vials during imaging, hence the reflections.

3.2. TEM and STEM/EDS Data. TEM micrograph collages are presented in Figure 3a−c for unthiolated samples (i.e., HTX, HTX-Ag^+, and HTX-Ag^0) and in Figure 3d−f for thiolated samples (i.e., HTX-SH, HTX-S-Ag^+, and HTX-S-Ag^0). For all samples, the fractal geometries observed are common in these types of porous Ag−Al−Si−O gel-based substrates.[18,23,50,51] Both thiolated and unthiolated gels with Ag^+ and Ag^0 forms of silver showed evidence of less electron-transparent and somewhat spherical regions indicative of high silver, which were confirmed with STEM−EDS maps shown in Figure S5 (Supporting Information). Figure S5 (Supporting Information) also shows homogeneous elemental distributions for all of the expected species in the different samples.

3.3. XPS Data. XPS analysis was used to probe the near-surface chemical speciation of the Ag-xerogel materials. The survey spectra on the Ag-substituted xerogels do not show the presence of a Na 1s feature, signifying a high degree of Ag-substitution for Na in the materials (i.e., Na is below the XPS detection limits)—see Figure S1 (Supporting Information). In the thiolated Ag-xerogels, the S 2p feature reveals that sulfur is primarily present as a thiol (i.e., S^{2-}) species, likely bound to silver, as evidenced by BE of 162.9 eV. A small amount of sulfate (i.e., SO_4^{2-}) was also present in both thiolated xerogels with a BE of 168.3 eV for the S $2p_{3/2}$ feature and was attributed to oxidation of near-surface thiol groups.

Probing Ag speciation using XPS is known to be quite challenging.[17,45] Although assigning oxidation states based solely on the BE of the Ag $3d_{5/2}$ feature can lead to erroneous conclusions, it has been shown that the MAP can be used to differentiate between reduced (i.e., Ag^0) and oxidized (i.e., Ag^+) silver species.[45] Therefore, in the current work, a combination of MAP values and peak-deconvoluted Ag 3d features were used to assign plausible Ag-oxidation states, which were then correlated with results obtained from other analytical techniques (e.g., XRD and TEM). The MAP values for Ag were calculated using the formula presented in eq 7, and these values are listed in Table S2 (Supporting Information). It is known from previous reports that oxidized Ag species exhibit a lower MAP value compared to a Ag^0 species.[45] From Table S2 (Supporting Information), it is clear that both the Ag-substituted xerogels exhibit a notably lower MAP value compared to the reduced analogues (see Figures S2 and S3, Supporting Information). This points to a successful reduction step where the reduced Ag^0-xerogels (i.e., HTX-Ag^0 and HTX-S-Ag^0) have higher Ag^0 concentrations

https://doi.org/10.1021/acsanm.2c01741
ACS Appl. Nano Mater. 2022, 5, 9478−9494

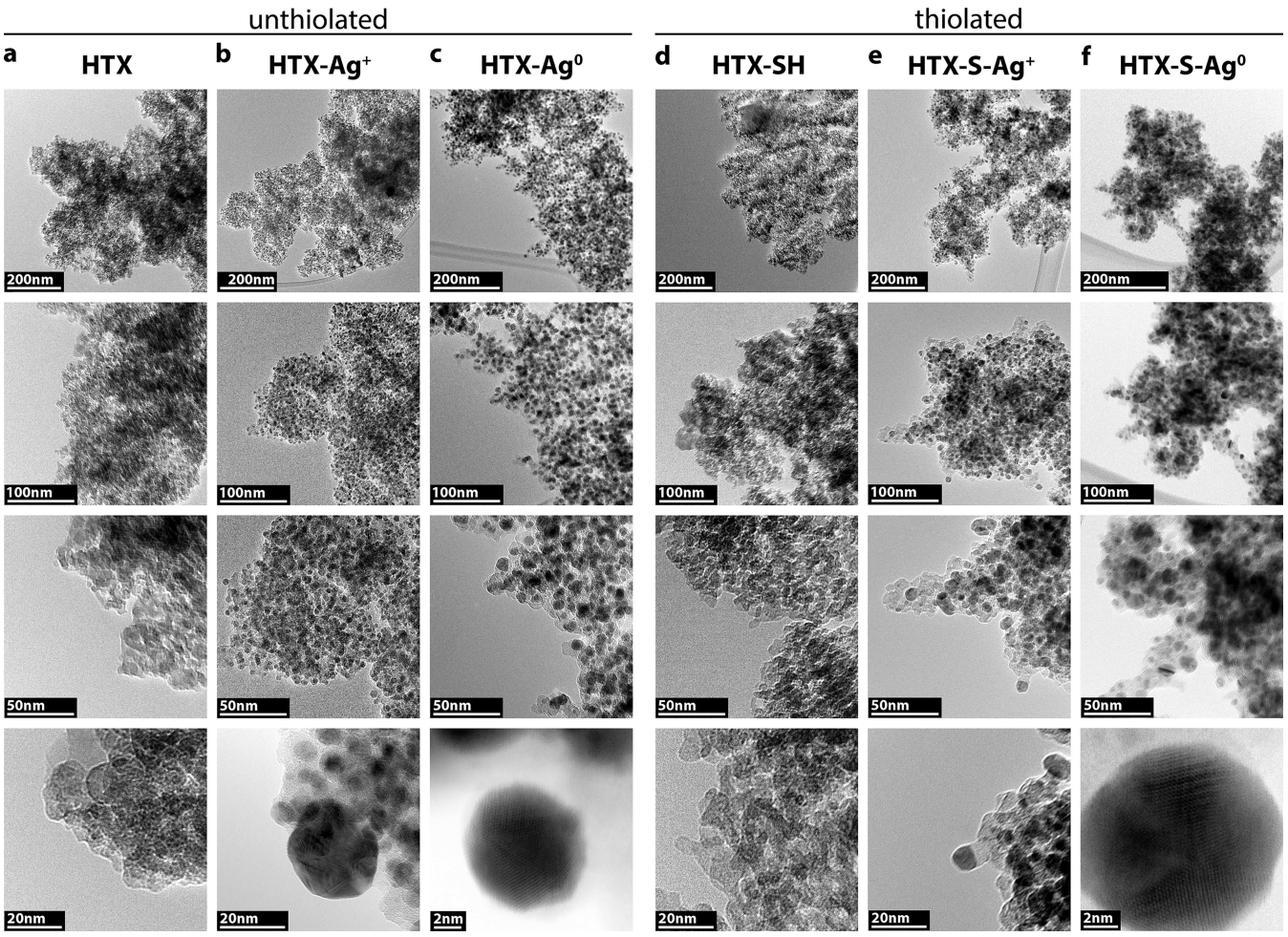

Figure 3. TEM collage showing progressively higher magnifications from top to bottom for (a–c) unthiolated samples (a) HTX, (b) HTX-Ag^+, and (c) HTX-Ag^0 and (d–f) thiolated samples (d) HTX-SH, (e) HTX-S-Ag^+, and (f) HTX-S-Ag^0.

compared to the equivalent Ag^+-exchanged versions of the samples (i.e., HTX-Ag^+ and HTX-S-Ag^+), respectively.

Following these processes and calculations, the Ag 3d features were deconvoluted to allow for a better understanding of the distribution of Ag-oxidation states in the materials, and these deconvolutions are shown in Figure 4. The Ag $3d_{5/2}$ feature for HTX-Ag^+ was fit using two major components at BEs 368.4 and 368.8 eV (Figure 4a), and HTX-S-Ag^+ also had two primary components at similar BEs of 368.5 and 368.9 eV (Figure 4c). The components at ~368.8 eV were assigned to Ag^0 species, while the lower-BE components ~368.4 eV were attributed to Ag^+ species. The presence of both Ag^0 and Ag^+ species in the Ag-exchanged materials was verified with XAS data described below in more detail. Here, although the BEs of Ag^0 species were slightly higher than that observed for bulk Ag foil (see Tables S1 and S2, Supporting Information), these differences can be attributed to the size effect of Ag^0 on its BE. It has been shown in the previous reports[17,52] that ~6 nm Ag^0 nanoparticles exhibit a BE of approximately ~368.8 eV, while those around 2 nm have an even higher BE of ~369.1 eV or greater. These values are in excellent agreement with XRD analysis that reveals a bimodal distribution of Ag^0 nanoparticles of sizes ~6 and ~2 nm (vide infra), as shown in Table S9 (Supporting Information). Additionally, these values also agree well with crystallites observed during TEM observations discussed in later sections. Upon reduction, the Ag $3d_{5/2}$ peak shifts to a slightly higher BE value. When peak-fitting the Ag 3d feature of the HTX-Ag^0 material, the primary component in the Ag $3d_{5/2}$ region was found to have a BE of 368.7 eV, which was attributed to Ag^0 species (Figure 4b). The component at a higher BE of 369.4 eV also possibly represents Ag^0 nanoparticle but of a smaller size (<2 nm). Similar results were also obtained for the HTX-S-Ag^0 material, which was also found comprised of Ag^0 species (Figure 4d). These results align well with that concluded using MAP values, where the reduced Ag-xerogels were found to consist of Ag^0 species. The most prevalent sulfur species found in both HTX-S-Ag^+ (Figure 4e) and HTX-S-Ag^0 (Figure 4f) were thiols with smaller amounts of sulfate present in each sample.

Finally, BE peak shifts toward higher energies were observed in Si 2p, Al 2p, and O 1s regions between HTX-Ag^+ and HTX-Ag^0 (see Figure S4, Supporting Information). This is likely due to subtle changes in the bonding environments for charge compensation after the $Ag^+ \rightarrow Ag^0$ reduction process.

3.4. BET Data. The SSA data from BET measurements are provided in Figure 5, and isotherms as well as the pore size distribution plots are presented in Figure S6 (Supporting Information). As expected, every subsequent treatment after the as-made xerogel lowered the SSA values. The thiolation process did not notably reduce the SSA from the HTX starting material (i.e., 313 $m^2\ g^{-1}$ for HTX → 294 $m^2\ g^{-1}$ for HTX-SH; or ~6%), whereas when a similar process was performed for heat-treated Na–Al–Si–O aerogels (HTA) of the same target composition,

https://doi.org/10.1021/acsanm.2c01741
ACS Appl. Nano Mater. 2022, 5, 9478–9494

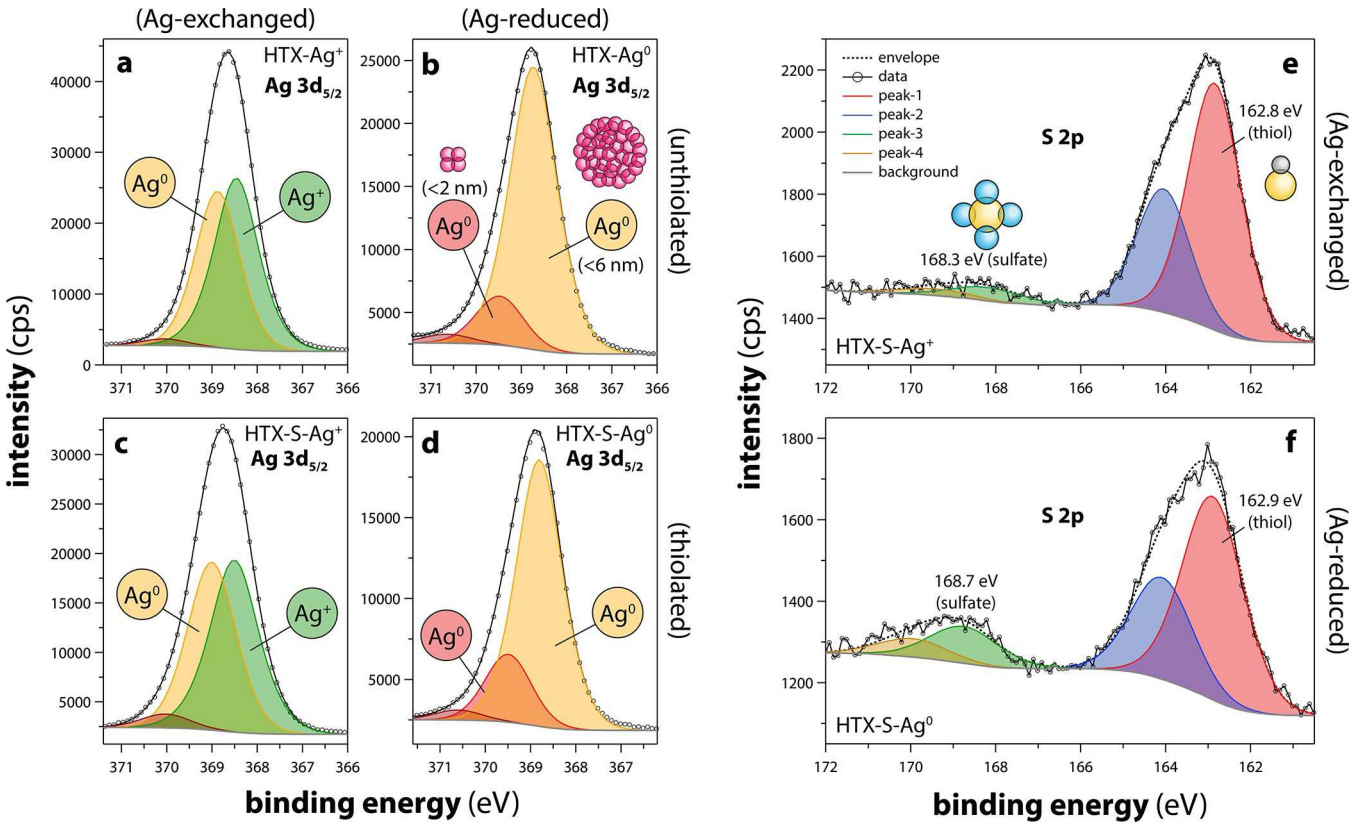

Figure 4. (a–d) XPS of the Ag $3d_{5/2}$ region for (a) HTX-Ag^+, (b) HTX-Ag^0, (c) HTX-S-Ag^+, and (d) HTX-S-Ag^0. The yellow area denotes Ag^0 at <6 nm diameter (estimated), red denotes Ag^0 at <2 nm diameter (estimated), and green denotes Ag^+; examples of differently sized Ag^0 clusters are shown in the form of molecular drawings in (b). Refer to the online version for color references. (e,f) XPS data showing spectra of the S 2p region for (e) HTX-S-Ag^+ and (f) HTX-S-Ag^0 along with peak deconvolution for both spectra; molecular drawings are provided for sulfate (SO_4^{2-}) and thiol (SH) groups. The background is gray for all fits.

the same thiolation process resulted in an SSA decrease of >90% from 291 to 28 $m^2\ g^{-1}$ (HTA-SH).[23] A comparison of the xerogels from the current study with aerogels of the same composition (i.e., Ag–Al–Si–O) from our previous study[23] is provided in Figure S7 (Supporting Information), which shows that while the as-made aerogel had a much higher SSA value compared to the as-made xerogel, the SSA of the xerogel was notably higher after the HT process and at all subsequent steps.

Thus, while the xerogels had only marginally higher SSA values for unthiolated gels over equivalent aerogels (i.e., 1.1–1.2×),[23] the thiolated xerogels showed 3.6–10.5× higher SSA values compared to thiolated aerogels, providing evidence that the xerogels are much less susceptible to pore structure collapse during processes such as the heat treatment (HT), thiolation (SH), silver loading (Ag^+), and silver reduction (Ag^0). This is another demonstration of how the xerogels provide a far more rigid scaffold for subsequent processes required to prepare these types of sorbents.

3.5. Appearance (after Iodine Loading). Pictures of the iodine-loaded gels are provided in Figure S10 (Supporting Information). The iodine-loaded HTX, that is, HTX(+I), was mostly unchanged but had a slightly off-white color. The HTX-Ag^+(+I) and HTX-Ag^0(+I) looked very similar and a bright yellow in color. The iodine-loaded HTX-SH, or HTX-SH(+I), was white with dark gray/black patches on various locations of certain granules. The HTX-S-Ag^+(+I) granules looked similar to the unthiolated equivalent samples but were a lighter yellow. The HTX-S-Ag^0(+I) granules were a darker yellow than the other Ag-loaded sorbents with small patches of brown.

3.6. Sample Densities. The skeletal pycnometric densities for X, HTX, HTX-Ag^+, HTX-Ag^0, HTX-SH, HTX-S-Ag^+, and HTX-S-Ag^0 are shown in Figure S9 and Table S5 (Supporting Information). The ρ value for HTX was slightly higher than the value for X, which is likely due to the desorption of residual hydrocarbons present in the X sample (from the gel synthesis process) and adsorbed water during the HT process to form HTX. This hydrocarbon removal was observed for HTs on Na–Al–Si–O aerogels in our previous work.[23] The value for HTX-SH was slightly lower, which is due to the addition of the thiolpropyl monolayers added to the HTX gel during the thiolation process, which are lower in density than the base gel. Adding silver to the base materials notably increased ρ values (~53–72%; see $\Delta\rho_{(base\rightarrow Ag)}$ values in Table S5, Supporting Information) where the thiolated gels were consistently lower than the unthiolated equivalents (i.e., HTX-Ag^+ > HTX-S-Ag^+ and HTX-Ag^0 > HTX-S-Ag^0). These differences were also attributed to the addition of the thiolpropyl monolayers on the thiolated gels. In each case, the Ag^0 samples had slightly higher ρ values than the equivalent Ag^+ samples (i.e., HTX-Ag^0 > HTX-Ag^+ and HTX-S-Ag^0 > HTX-S-Ag^+), and this could be due to the removal of other adsorbed species in the Ag^+ gels during the Ag^0 reduction process performed under H_2/Ar. All Ag-containing samples showed higher densities after iodine loading, and the thiolated gels showed higher relative ρ increases (22–25%) than the unthiolated gels (9–13%) (see $\Delta\rho_{(Ag\rightarrow AgI)}$ values in Table S5, Supporting Information).

3.7. XRD Data. The raw XRD spectra are provided in Figures S13–S24 (Supporting Information). A summary of the XRD

https://doi.org/10.1021/acsanm.2c01741
ACS Appl. Nano Mater. 2022, 5, 9478–9494

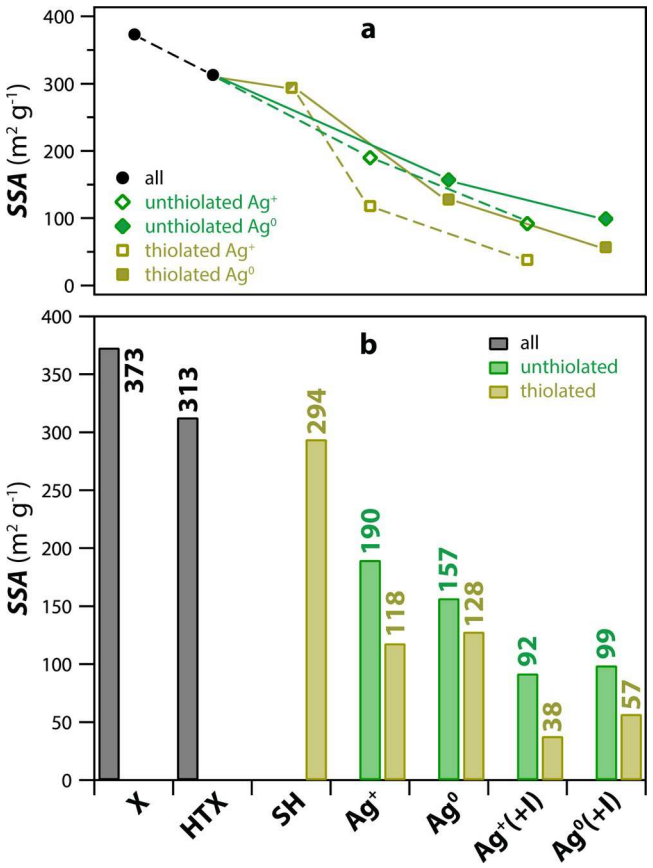

Figure 5. BET data showing the data (a) plotted with lines drawn between like series and (b) column chart showing the data. The *x*-axis is the same for both (a,b).

data is provided in Figure 6 where background intensities were removed for each data set. The amorphous structure of the X and HTX samples was similar to broad diffraction peaks that represent the amorphous structure of these samples (Figure 6a). No diffraction, including any broad amorphous diffraction peaks, was observed for HTX-SH (Figure 6d). The diffraction patterns for HTX-Ag^+, HTX-Ag^0, and HTX-S-Ag^0 showed peaks for Ag^0 (see Figure 6c–f). Rietveld refinements were performed for HTX-Ag^0 and HTX-S-Ag^0 and show very low residuals (R_{wp} values)[47] after two separate Ag^0 phases were used including a cubic (space group $Fm\bar{3}m$) and a hexagonal (space group $P6_3/mmc$)—see Figure 6e,f. Table S9 (Supporting Information) provides a list of the crystallite sizes determined with the refinements, and both show majority phases of cubic Ag^0 (>85 mass %) with average crystallite sizes of ~6.6 nm and minority phase of hexagonal Ag^0 (<15 mass %) with average crystallite sizes of ~1.9–2.7 nm in diameter. In our previous work with thiolated Ag^0–Al–Si–O aerogels, only the cubic $Fm\bar{3}m$ phase was used for fitting, and the sizes were similar when measured by Rietveld refinements of XRD scans (7.4 nm) and when measured from TEM micrographs (5.9 ± 1.4 nm).[23] For all four of the iodine-loaded samples, a mixture of β-AgI (space group 186, $P6_3mc$)[53] and γ-AgI (space group 216, $F\bar{4}3m$)[54] was observed, which is consistent with our previous work.[23,32,50,51]

3.8. EDS Data. The EDS data for all samples are provided in Table S8 (Supporting Information) in addition to calculations like AgU values and Si/Al molar ratios. The samples showed very high iodine loadings of 45.5, 44.9, 47.9, and 47.8 mass % iodine for samples HTX-Ag^+(+I), HTX-Ag^0(+I), HTX-S-Ag^+(+I), and HTX-S-Ag^0(+I), respectively, where the thiolated samples showed higher values for both the Ag^+ and Ag^0 samples. The AgU values for HTX-Ag^+(+I), HTX-Ag^0(+I), HTX-S-Ag^+(+I), and HTX-S-Ag^0(+I) were 1.12, 1.02, 1.18, and 1.16, respectively, where Ag^+ samples showed higher values than Ag^0 samples. The addition of 3-MPTMS to the gels notably increases the Si loadings in all samples due to the addition of the Si in the 3-MPTMS where the Si/Al molar ratios are all increased by an average of 31 ± 7% between unthiolated and thiolated samples after the same treatments; this is shown graphically in Figure S11 (Supporting Information).

3.9. XAS Data. A summary of the Ag K-edge XANES data is provided in Figure 7a–h. The analysis presented in Table S4 (Supporting Information) shows the quantitative data of the various Ag-containing phases used to fit the XANES data. These data show the majority phase for HTX-Ag^+, HTX-Ag^0, HTX-S-Ag^+, and HTX-S-Ag^0 (i.e., samples without iodine) matched that of the Ag-MOR standard with actively reduced materials containing some Ag^0 and Ag_2O. In the HTX-Ag^+, HTX-S-Ag^+, and Ag-MOR XANES spectra, only one spectral feature is visible just after the absorption edge, demonstrating that the Ag^+ species must be present in channels or cages in the aluminosilicate network, which leads to large positional disorder of Ag ions and therefore relatively few spectral features, as previously described by Abney et al.[43] The Ag_2O fractions in thiolated samples (i.e., HTX-S-Ag^+ and HTX-S-Ag^0) showed higher Ag_2O content than the unthiolated versions of these samples (i.e., HTX-Ag^+ and HTX-Ag^0). The Ag^0/Ag^+ content ratio was higher for HTX-Ag^0 versus HTX-S-Ag^0.

A summary of S K-edge XANES data is provided in Figure 7i. The location of various S-based species with different oxidation states can be seen in distinctly different locations within XANES spectra, as shown roughly by the vertical bars in Figure 7i. In this case, all samples without iodine showed better qualitative overlap to S^{2-} (i.e., Ag_2S) species than to the SO_4^{2-} (i.e., $CaSO_4$) species, whereas the opposite was true for iodine-loaded samples.

A summary of I L_3-edge XANES data is provided in Figure 7j. For these data, all Ag-exchanged samples showed a qualitative fit with AgI, and this included HTX-Ag^+, HTX-Ag^0, HTX-S-Ag^+, and HTX-S-Ag^0. The HTX-S sample that did not undergo Ag^+ exchange showed a better fit with NaI than the other I-containing standards analyzed. This suggests that the iodine bonded to Na^+ present in these samples (see Table S8 in the Supporting Information), but the XRD data do not show the presence of crystalline NaI.

3.10. SAXS Data. Figure S8 (Supporting Information) provides the SAXS data for 10 samples including HTX, HTX-Ag^+, HTX-Ag^0, HTX-Ag^+(+I), HTX-Ag^0(+I), HTX-SH, HTX-S-Ag^+, HTX-S-Ag^0, HTX-S-Ag^+(+I), and HTX-S-Ag^0(+I). A broad peak can be seen in the SAXS data for several samples centered near q = 0.08 $Å^{-1}$ (where q is the magnitude of the momentum transfer vector) indicating the presence of Ag^0 nanoparticles with a corresponding average particle diameter of 7.9 nm, based on the relationship of $d = 2\pi/q$ where d is the particle diameter in nm, which corresponds well with the data shown in Figure 6e,f and Table S9 (Supporting Information). The remaining Ag-containing samples appear to have some indication of a scattering signal; however, these signals were shifted to lower q, which corresponds to larger average particle sizes. However, the SAXS instrumentation was not optimized to measure correlations at this low q range and would necessitate ultra-small-angle X-ray scattering (USAXS). The SAXS data of

https://doi.org/10.1021/acsanm.2c01741
ACS Appl. Nano Mater. 2022, 5, 9478–9494

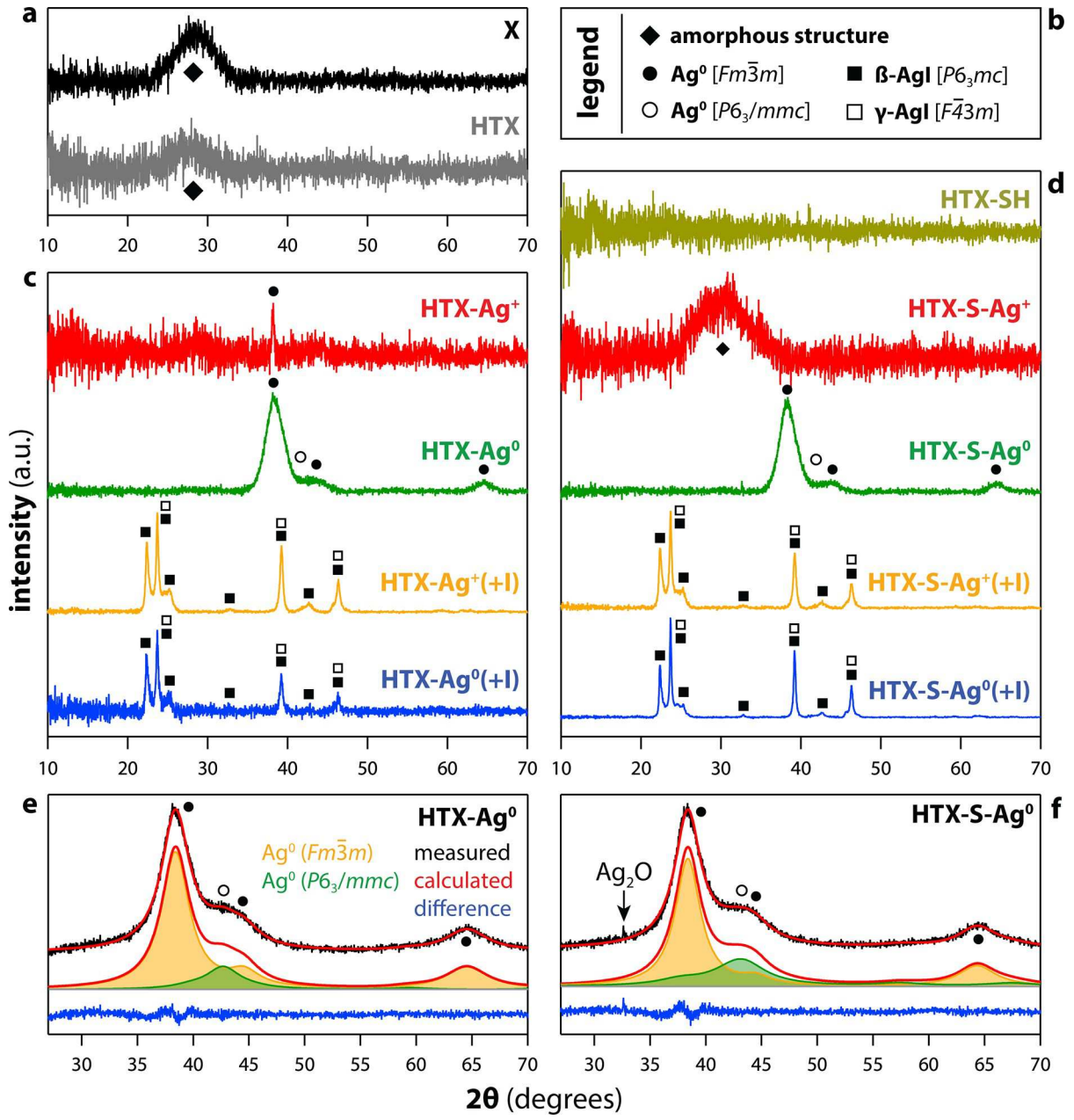

Figure 6. XRD data including (a) X and HTX, (c) unthiolated gels HTX-Ag^+, HTX-Ag^0, HTX-Ag^+(+I), and HTX-Ag^0(+I), and (d) thiolated gels HTX-SH, HTX-S-Ag^+, HTX-S-Ag^0, HTX-S-Ag^+(+I), and HTX-S-Ag^0(+I). (b) Legend showing what phases the symbols represent in other subfigures. Common sample treatments are aligned vertically for unthiolated and thiolated samples. (e,f) Summary of Rietveld fitting of XRD data from Ag^0 (i.e., $Fm\bar{3}m$ and $P6_3/mmc$) present in the Ag-reduced samples including (e) HTX-Ag^0 and (f) HTX-S-Ag^0. Data from these fits are shown in Table S9 (Supporting Information).

HTX show the presence of at least one peak, the largest of which is centered near 0.01 $Å^{-1}$ (~63 nm), suggesting the presence of ~60 nm particulates in the HTX sample, which is similar to the TEM shown in Figure 3a where the particles are denoted as the agglomerates of the gel material, and the matrix is air. This is in contrast to Ag-containing material where the particles are likely the Ag^0 crystal agglomerates, and the matrix is either (1) the gel or (2) gel + air depending on the way the X-rays interact with these different material phases and the interfaces between them. After thiolation, the peak for the HTX-SH sample is shifted toward 0.09 $Å^{-1}$ (~7 nm).

4. DISCUSSION

An overview of which characterization techniques were performed on each sample is provided for convenience in Table S10 (Supporting Information). Based on the XRD, XPS, and TEM data, molecular drawings are provided in Figure 8 that show the generalized structure of the thiolated materials and how the 3-MPTMS groups tether to the xerogel network (Figure 8a,b). The Ag^0 crystallites in actively reduced sorbents were present in various sizes with sphere-like clusters of varying sizes that appeared to be polycrystalline with different lattice orientations (see Figures 3c,f, 4b,d, 6e,f, 8e, and Table S9 in the Supporting Information). These types of information are essential for designing future sorbents and optimizing the

https://doi.org/10.1021/acsanm.2c01741
ACS Appl. Nano Mater. 2022, 5, 9478−9494

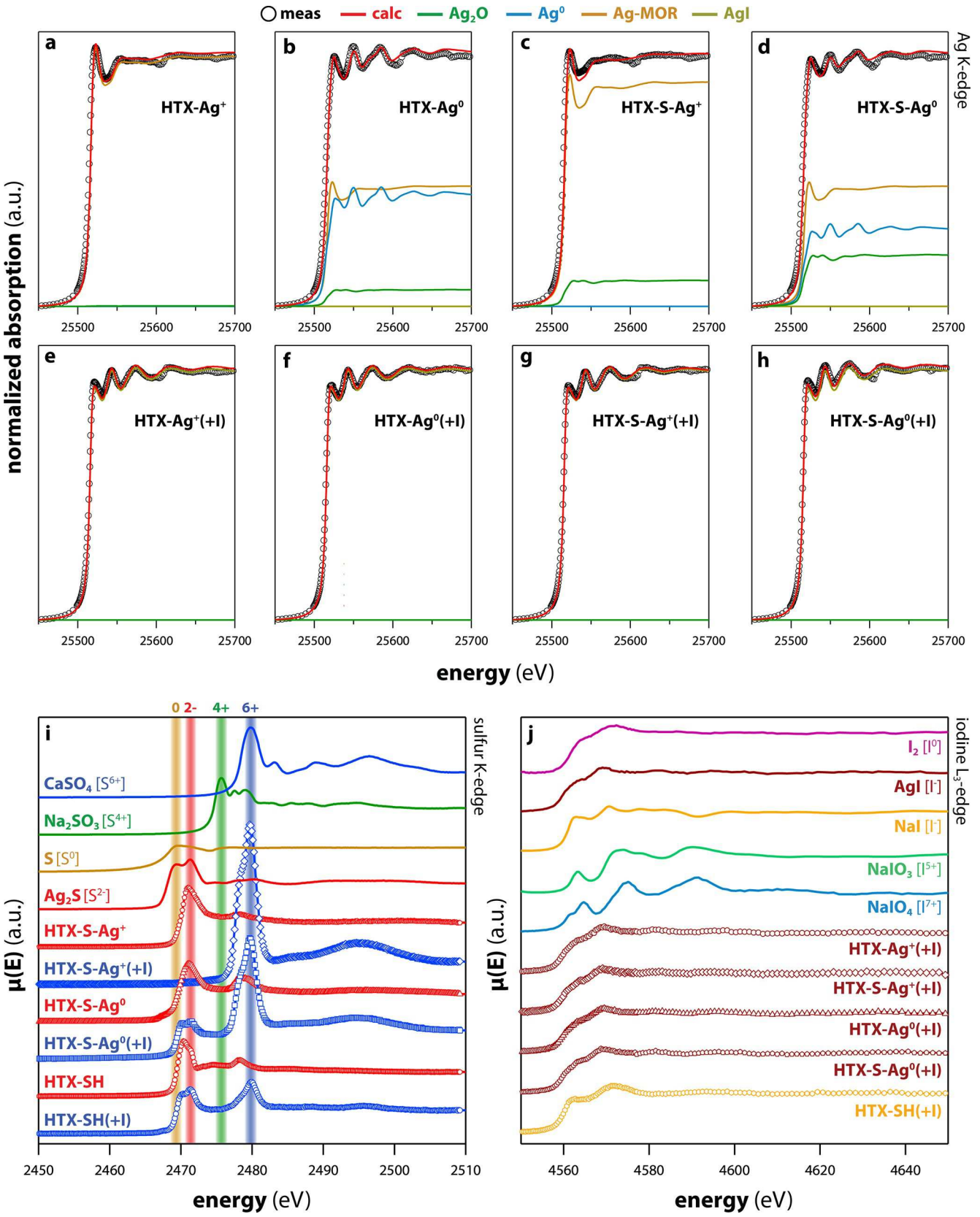

Figure 7. (a–h) Silver K-edge XANES data for (a) HTX-Ag^+, (b) HTX-Ag^0, (c) HTX-S-Ag^+, (d) HTX-S-Ag^0, (e) HTX-Ag^+(+I), (f) HTX-Ag^0(+I), (g) HTX-S-Ag^+(+I), and (h) HTX-S-Ag^0(+I) as well as (i) sulfur K-edge XANES and (j) iodine L_3-edge XANES for all samples.

materials for having the desired oxidation states for the getter (e.g., Ag^+ vs Ag^0) as well as any tether being implemented (e.g., thiol vs sulfate). Figure 8d also provides an overview of how the sulfur species are expected to bond to the sorbents and how they might change upon oxidation (i.e., thiol groups → sulfate groups).

https://doi.org/10.1021/acsanm.2c01741
ACS Appl. Nano Mater. 2022, 5, 9478−9494

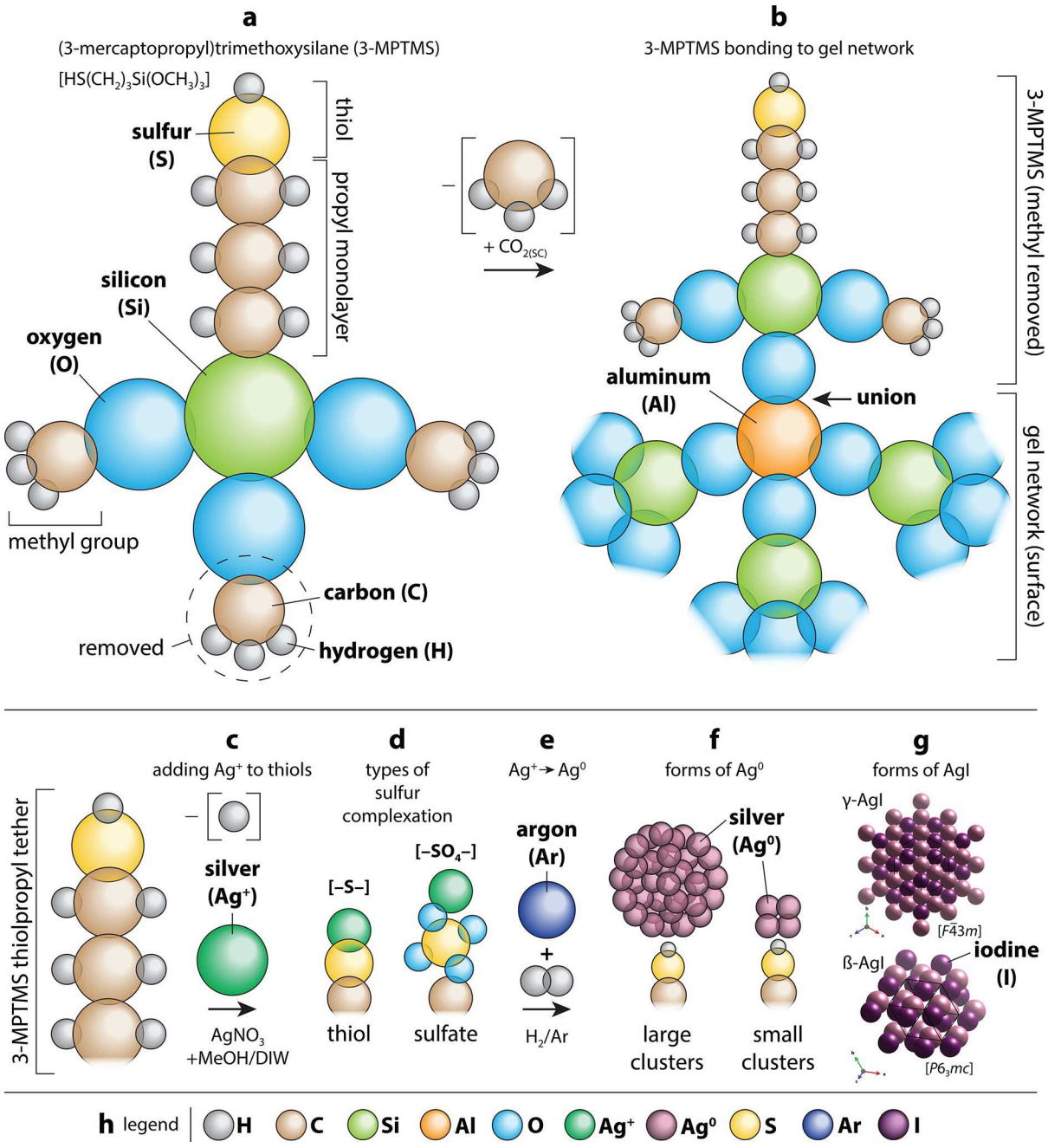

Figure 8. Summary of how 3-MPTMS [shown in (a)] interacts with the gel network [shown in (b)] showing the union between the 3-MPTMS and the xerogel. (c) Summary of how Ag^+ interacts with the thiol group, (d) sulfur complexation, (e) how Ag^+ is reduced to Ag^0, (f) how the Ag^0 crystals form around the thiol group and on the surface of the gel, as confirmed by various characterizations described in the text, (g) forms of AgI that are created upon iodine chemisorption, and (h) the legend. Atoms are not drawn to scale.

The structures of the Ag^0 crystallites and the AgI crystallites seem to follow similar crystallographic trends of cubic and hexagonal Bravais lattices, which are shown graphically in Figures 8g and 9 (also see Figures 3, 6, and Table S9 in the Supporting Information). This suggests that it is possible that nanoscale cubic Ag^0 ($Fm\bar{3}m$) crystals convert to cubic γ-AgI ($F\bar{4}3m$) and hexagonal Ag^0 ($P6_3/mmc$) crystals convert to hexagonal β-AgI ($P6_3mc$), which could be explored more in the future.

It should be noted that linear combination fitting of XANES data of HTX-Ag^+ does not exactly corroborate the XPS findings. It should be noted that a similar fraction of Ag^+ prior to reduction by H_2 in Ag-MOR was reported by Abney et al.[43] where the local structure of Ag in Ag-MOR varied significantly before and after reduction by H_2. However, few studies have attempted to understand the oxidation state of silver through both XPS and XANES. The XANES measurements, which were performed in both fluorescence and transmission modes, represent a bulk characterization method because the material was crushed and mixed with a binder while the XPS data represent a surface-sensitive characterization method. Additionally, XANES measurements are performed using a high X-ray flux in air, and XPS measurements are performed under an ultrahigh vacuum, both of which affect the oxygen fugacity, particularly for redox-sensitive species. Previous investigations of silver oxidation states for electrochemical reduction of CO_2

https://doi.org/10.1021/acsanm.2c01741
ACS Appl. Nano Mater. 2022, 5, 9478−9494

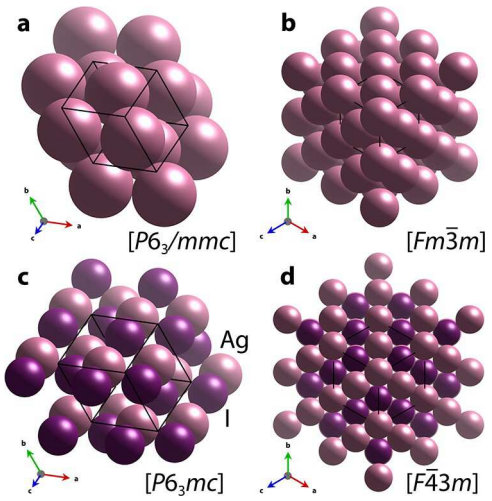

Figure 9. Crystal structures of Ag^0 and AgI including (a) hexagonal Ag^0 in the $P6_3/mmc$ space group, (b) cubic Ag^0 in the $Fm\bar{3}m$ space group, (c) hexagonal β-AgI in the $P6_3mc$ space group, and (d) cubic γ-AgI in the $F\bar{4}3m$ space group. The same orientations are shown for both cubic and hexagonal space groups separately.

through XPS suggest that the levels of vacuum may convert Ag−O to Ag^0.[55] On the other hand, when Ag^0 is present as nanoscale crystallites, the high-surface area may enhance the ability to oxidize in air when irradiated with the synchrotron X-rays and artificially increase the fraction of Ag^+ in these samples. In general, XPS tended to demonstrate a higher fraction of Ag^0, whereas XANES demonstrated a higher fraction of Ag^+.

A comparison of iodine-loading capacities in terms of q_e [i.e., mg iodine per g of the sorbent or 1000·(g g^{-1}), a modification of eq 4] for various Ag-based sorbents is provided in Figure 10 with the full data set provided in Table S11 (Supporting Information).[23,32,56−60] This comparison includes Ag-based sorbents that were loaded in the same manner under similar saturated conditions in our laboratory using a 1 L Savillex PFA jar for 24 h followed by 1 h of desorption. The comparison includes two zeolites including Ag-MOR (IONEX Ag-900 mordenite) and AgX (IONEX Ag-400 faujasite), both in the form of engineered particles from Molecular Products with proprietary clay binders. The data from a previous study was used for Ag-MOR since the values were higher (q_e = 131 mg g^{-1}) than those presented in Table S11 (Supporting Information) from the current study (q_e = 90.4 mg g^{-1}). This comparison has data from a recent study[32] of pure Ag^0 metal wire with a value of q_e = 1192 mg g^{-1}, which is close to that of the expected theoretical maximum (q_e = 1176 mg g^{-1}) assuming full chemisorption to form AgI from all of the available Ag^0 present. This figure also provides a direct head-to-head comparison of Ag−Al−Si−O aerogels from a previous study[23] with the xerogel equivalents, including unthiolated and thiolated versions of both Ag-exchanged (Ag^+) and Ag-reduced (Ag^0) samples. All of the Ag−Al−Si−O samples outperform the zeolite sorbents. For the unthiolated Ag−Al−Si−O sorbents, both the Ag^+ and Ag^0 aerogels showed higher q_e values than the xerogel equivalents, but this was reversed for the thiolated versions. Since these sample batches were made at vastly different times, it is difficult to compare them directly, but these discrepancies could be due to differences in Ag contents or thiol loadings. These types of comparisons show the data gaps that can help guide the development of next-generation sorbents with nanoscale functionalization for these types of applications.

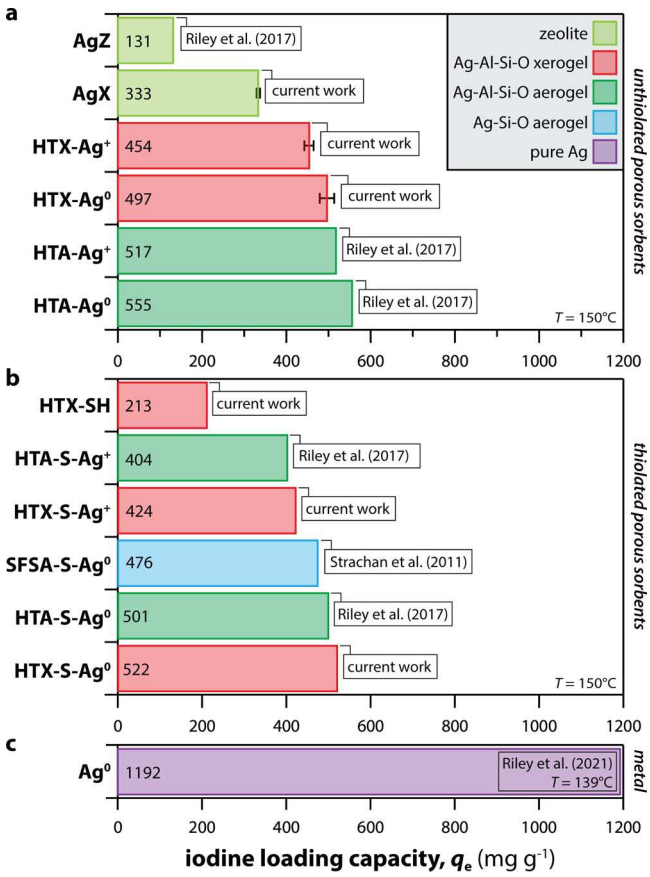

Figure 10. Summary of iodine-loading capacities (q_e in mg g^{-1}) in saturated conditions for Ag-based materials in categories of (a) unthiolated porous sorbents, (b) thiolated porous sorbents, and (c) pure Ag^0 metal.[32] Sorbents include AgZ (IONEX Ag-900 silver mordenite),[23] AgX (IONEX Ag-400 silver faujasite; see Table S7, Supporting Information), silver-functionalized silica aerogel (SFSA-S-Ag^0),[60] Ag−Al−Si−O aerogels,[23] thiolated Ag−Al−Si−O aerogels,[23] as well as thiolated and unthiolated Ag−Al−Si−O xerogels from the current work. For the Ag−Al−Si−O samples, both silver-loaded (Ag^+) and silver-reduced (Ag^0) samples are included separately for comparison. Temperatures utilized for the iodine-loading procedure are listed in each plot separately (i.e., 139 or 150 °C). All loadings were conducted for 24 h in a 1 L Savillex PFA jar. The data used in this figure are included in Table S11 (Supporting Information). For pure Ag^0, the theoretical maximum chemisorption potential for iodine assuming full conversion of $2Ag + I_{2(g)} \rightarrow 2AgI$ is q_e = 1176 mg g^{-1}; therefore, anything over that value is likely physisorbed iodine.

Data not included in Figure 10 include that Ag-based sorbents run under different conditions such as the Ag−Ni foam by Tian et al.[61] with a reported q_e = 442 mg g^{-1} (T = 200 °C, t = 4 h). Additionally, several other sorbent types could be included here such as Bi-based materials. For instance, recent studies showed q_e values of 351 mg g^{-1} for Bi-functionalized silica aerogel (i.e., BFSA),[62] 618.9 mg g^{-1} for a Bi−Ni foam,[61] and 732 mg g^{-1} for a Bi-based electrospun sorbent (i.e., HT-Bi-ESCNF, 200 °C).[63] Utilizing getters with higher metal oxidation states for the metal-iodide form like bismuth (i.e., Bi^{3+} in BiI_3) means a higher theoretical iodine capacity for the same starting moles of a lower oxidation state metal like Ag (i.e., Ag^+ in AgI); of course, this assumes full utilization of the getter metal. However, this approach could have tradeoffs when it comes to the final disposition pathway for the iodine-loaded sorbents since the water solubility of AgI is very low (i.e., 3×10^{-6} g per 100 g of

https://doi.org/10.1021/acsanm.2c01741
ACS Appl. Nano Mater. 2022, 5, 9478−9494

water) and outperforms most other metal-iodide complexes including BiI_3 (i.e., 7.8×10^{-4} g per 100 g of water) and CuI (i.e., 2×10^{-5} g per 100 g of water).[42,64]

A wider range of both inorganic and organic sorbents that rely on physisorption and/or chemisorption mechanisms to scavenge iodine is provided in Table S13 (Supporting Information),[32,65−69] and readers are referred elsewhere for more comprehensive reviews of sorbent lists from the literature for this application.[3,4,70] In this comparison, it is clear that inorganic sorbents relying solely on chemisorption-based processes show much lower iodine capacities than those that utilize physisorption or both chemisorption and physisorption. However, it is likely that the pathway to disposal for chemisorption-only sorbents will be easier since they can often be hot-pressed (volume-reduced) into monolithic waste forms for storage in a waste repository, whereas loosely bound iodine will probably volatilize off during hot pressing. Sorbents that only physisorb iodine could potentially require iodine release and subsequent recapture prior to long-term disposal in a repository as, if left in the original adsorbed state, iodine might desorb over geologic timescales or if the storage environment changes (e.g., increases in temperature). Finally, adding additional processing steps into nuclear facilities can lead to drastic increases in cost, especially over long plant operation lifetimes and large-scale material handling, so a limited-step capture and disposal process is more attractive from that perspective.

The data generated from this study revealed the limitations of analyzing these types of porous and redox-sensitive sorbents with different techniques. Some analysis techniques were performed under vacuum in the absence of air (e.g., SEM, EDS, TEM, and XPS), whereas others were performed at atmospheric pressure (e.g., XRD, XANES, and density) in the presence of air where Ag-redox (i.e., Ag^+/Ag^0 ratio) and bonding environments (e.g., Ag_2O vs Ag-MOR) are subject to change. Oxygen-containing environments that could accelerate the conversion of reduced Ag^0 toward more oxidized species (e.g., Ag_2O and Ag-MOR), especially in experimental conditions that require high energies and fluxes such as those performed as synchrotron facilities (e.g., SAXS and XAS), might change the samples from the original state to something nonrepresentative.

5. SUMMARY AND CONCLUSIONS

Several key pieces of information were gained during this study including the following: (1) using HTX substrates for thiolation significantly reduced the pore structure collapse of the base material over what was observed for aerogel equivalent samples, (2) two types of nanoscale Ag^0 crystals are formed during the Ag-reduction process that include ∼6−7 nm cubic (space group $Fm\bar{3}m$) and a ∼2−3 nm hexagonal (space group $P6_3/mmc$) crystals based on XPS and XRD data, (3) based on XPS data, both HTX-Ag^+ and HTX-S-Ag^+ samples contained some Ag^0 on the order of ∼50% (with the rest being Ag^+) where HTX-Ag^0 and HTX-S-Ag^0 samples showed complete Ag reduction to Ag^0, (4) XPS data showed thiol as the primary form of sulfur present in the thiolated samples (HTX-S-Ag^+ and HTX-S-Ag^0) with minor amounts of sulfate present, (5) this is the first account of documentation of size changes of our materials as a function of different treatment stages of hydrogel → alcogel → xerogel → HT process, and (6) thiolation did not notably change the iodine capacity over unthiolated sorbents under the conditions utilized in the current study. The q_e values for HTX-Ag^+(+I), HTX-Ag^0(+I), HTX-S-Ag^+(+I), and HTX-S-Ag^0(+I) were 454, 497, 424, and 522 mg g^{-1}, respectively, showing that the thiolation marginally improved the iodine capacity of Ag^0 gels (+5%) but decreased the capacity for Ag^+ gels (−6.6%). It should also be noted that thiolation using 3-MPTMS [i.e., $HS(CH_2)_3Si(OCH_3)_3$] adds Si to the gels and thereby increases the Si/Al molar ratio by 20−43%. These compositional shifts could play an important role in improving chemical durability of the final sorbent in different environments whereby the thiol groups can aid in delaying or maybe even preventing Ag-redox reactions until the thiol groups fully oxidize to sulfate groups. In addition, while thiolation might provide a redox buffer to slow the conversion of $Ag^0 \rightarrow Ag^+$, adding 3-MPTMS also installs hydrocarbons (propyl groups) that could complicate the consolidation process after iodine loading to produce a final waste form for disposal.

These data provide additional insights into the material properties as a function of the range of surface and bulk treatment processes utilized to fabricate the materials. However, based on a holistic view of the entire analytical data set, it is likely that some of the characterization techniques employed in this study altered the sample properties by changing Ag-redox states (i.e., due to high energy fluxes associated with synchrotron techniques). An important conclusion from this work is that these types of corroborative and noncorroborative data sets could be easily misinterpreted if the additional data sets were not collected. This finding provides justification for conducting parallel analyses to justify conclusions with porous redox-sensitive samples.

In situ evaluation of Ag^0 oxidation in different conditions representative of those expected in an off-gas facility using a variety of techniques (e.g., XAS, hot-stage XRD) would be an interesting way of evaluating the kinetics of this reaction for these sorbents. Also, to avoid the addition of propyl groups to the gel during thiolation, alternative approaches for installing thiol groups could be evaluated in the future. Using an approach that does not add unwanted SiO_2 molecules would also help because, at a fixed Ag-loading (based on the initial Na concentrations in the gel), adding these SiO_2 molecules this just dilutes the iodine capacities of the thiolated sorbents if only accounting for Ag-based iodine chemisorption. However, since the iodine capacity of HTX-S-Ag^0(+I) was higher than that of HTX-Ag^0(+I), this suggests that the thiol groups might play an important role in the iodine capture process and warrants further investigation.

■ ASSOCIATED CONTENT

Supporting Information

The Supporting Information is available free of charge at https://pubs.acs.org/doi/10.1021/acsanm.2c01741.

XPS data, STEM/EDS data, BET data, SAXS data, combination fitting data for XANES, density data, iodine-loading information for xerogel samples, iodine-loading information for Ag-FAU (IONEX Ag-400), EDS data, gel size comparisons, XRD data, summary showing which samples were analyzed with each technique, comparisons between Ag-based sorbents, and comparisons between non-Ag iodine sorbents (PDF)

■ AUTHOR INFORMATION

Corresponding Author

Brian J. Riley − *Energy and Environment Directorate, Pacific Northwest National Laboratory, Richland, Washington*

https://doi.org/10.1021/acsanm.2c01741
ACS Appl. Nano Mater. 2022, 5, 9478−9494

99354, United States; orcid.org/0000-0002-7745-6730; Email: brian.riley@pnnl.gov

Authors

Saehwa Chong − *Energy and Environment Directorate, Pacific Northwest National Laboratory, Richland, Washington 99354, United States;* orcid.org/0000-0002-4722-0022

José Marcial − *Energy and Environment Directorate, Pacific Northwest National Laboratory, Richland, Washington 99354, United States*

Nabajit Lahiri − *Physical and Computational Sciences Directorate, Pacific Northwest National Laboratory, Richland, Washington 99354, United States*

Mrinal K. Bera − *NSF's ChemMatCARS, Pritzker School of Molecular Engineering, The University of Chicago, Chicago, Illinois 60637, United States;* orcid.org/0000-0003-0698-5253

Sungsik Lee − *X-Ray Science Division, Argonne National Laboratory, Lemont, Illinois 60439, United States;* orcid.org/0000-0002-1425-9852

Tianpin Wu − *X-Ray Science Division, Argonne National Laboratory, Lemont, Illinois 60439, United States*

Karen Kruska − *Energy and Environment Directorate, Pacific Northwest National Laboratory, Richland, Washington 99354, United States*

Josef Matyáš − *Energy and Environment Directorate, Pacific Northwest National Laboratory, Richland, Washington 99354, United States;* orcid.org/0000-0003-2487-9219

Complete contact information is available at: https://pubs.acs.org/10.1021/acsanm.2c01741

Author Contributions

Conceptualization, B.J.R. and S.C.; methodology, B.J.R., S.C., J.M., N.L., M.K.B., S.L., T.W., and J.M.; validation, B.J.R., S.C., and J.M.; formal analysis, B.J.R., S.C., J.M., N.L., M.K.B., S.L., and T.W.; investigation, B.J.R., S.C., J.M., N.L., M.K.B., S.L., T.W., K.K., and J.M.; resources, B.J.R.; visualization, B.J.R., S.C., J.M., and N.L.; data curation, B.J.R., S.C., J.M., N.L., M.K.B., S.L., T.W., and K.K.; supervision, B.J.R.; writing—original draft preparation, B.J.R., S.C., J.M., N.L., M.K.B., S.L., T.W., K.K., and J.M.; writing—review and editing, B.J.R., S.C., J.M., N.L., and K.K.; and funding acquisition, B.J.R. All authors have read and approved the final version of the manuscript.

Notes

The authors declare no competing financial interest.

■ ACKNOWLEDGMENTS

The Pacific Northwest National Laboratory (PNNL) is operated by the Battelle Memorial Institute for the Department of Energy (DOE) under contract DE-AC05-76RL01830. This work was funded by the Department of Energy Office of Nuclear Energy. The authors are thankful to Ken Marsden at Idaho National Laboratory for programmatic support. Raman spectroscopy was performed using facilities at the Environmental Molecular Science Laboratory (EMSL, grid.436923.9), a DOE Office of Science User Facility sponsored by the Office of Biological and Environmental Research at PNNL. The authors thank Jacob Peterson and Jared Kroll for helping with the initial gel formulations to create the base materials used in this study as well as Carter Abney, Daniel Neuville, Rita Cicconi, and Georgia Cametti for sharing their measured XANES data. This research used resources of the Advanced Photon Source, a U.S. DOE Office of Science User Facility, operated for the DOE Office of Science by the Argonne National Laboratory under contract no. DE-AC02-06CH11357. NSF's ChemMatCARS Sector 15 is supported by the Divisions of Chemistry (CHE) and Materials Research (DMR), National Science Foundation, under grant number NSF/CHE-1834750. Extraordinary facility operations were supported in part by the DOE Office of Science through the National Virtual Biotechnology Laboratory, a consortium of DOE national laboratories focused on the response to COVID-19, with funding provided by the Coronavirus CARES Act.

■ REFERENCES

(1) Mattigod, S. V.; Serne, R. J.; Fryxell, G. *Selection and Testing of "Getters" for Adsorption of Iodine-129 and Technetium-99: A Review, PNNL-14208*; Pacific Northwest National Laboratory: Richland, WA, 2003.

(2) Haefner, D. R.; Tranter, T. J. *Methods of Gas Phase Capture of Iodine from Fuel Reprocessing Off-Gas: A Literature Survey, INL/EXT-07-12299*; Idaho National Laboratory: Idaho Falls, ID, 2007.

(3) Riley, B. J.; Vienna, J. D.; Strachan, D. M.; McCloy, J. S.; Jerden, J. L., Jr. Materials and Processes for the Effective Capture and Immobilization of Radioiodine: A Review. *J. Nucl. Mater.* **2016**, *470*, 307−326.

(4) Huve, J.; Ryzhikov, A.; Nouali, H.; Lalia, V.; Augé, G.; Daou, T. J. Porous Sorbents for the Capture of Radioactive Iodine Compounds: A Review. *RSC Adv.* **2018**, *8*, 29248−29273.

(5) Riley, B. J.; Chong, S. Environmental Remediation with Functional Aerogels and Xerogels. *Global Challenges* **2020**, *4*, 2070101.

(6) Riley, B. J.; McFarlane, J.; DelCul, G. D.; Vienna, J. D.; Contescu, C. I.; Forsberg, C. W. Molten Salt Reactor Waste and Effluent Management Strategies: A Review. *Nucl. Eng. Des.* **2019**, *345*, 94−109.

(7) González-García, C. M.; González, J. F.; Román, S. Removal Efficiency of Radioactive Methyl Iodide on TEDA-Impregnated Activated Carbons. *Fuel Process. Technol.* **2011**, *92*, 247−252.

(8) Maeck, W. J.; Pence, D. T. Application of Metal Zeolites to Radioactive Air Cleaning Problems. In*11th AEC Air Cleaning Conference, CONF-700816*; U.S. Atomic Energy Commission: Richland, WA, 1970; Vol. 2, pp 607−620.

(9) Pence, D. T.; Duce, F. A.; Maeck, W. J. Study of the Adsorption Properties of Metal Zeolites for Airborne Iodine Species Richland. In*11th AEC Air Cleaning Conference, CONF 700816*; Idaho Nuclear Corporation, 1970.

(10) Pence, D. T.; Duce, F. A.; Maeck, W. J. Developments in the Removal of Airborne Iodine Species with Metal Substituted Zeolites. In*12th AEC Air Cleaning Conference, CONF 720823*; Allied Chemical Corp: Oak Ridge, TN, 1973; p 417.

(11) Chapman, K. W.; Chupas, P. J.; Nenoff, T. M. Radioactive Iodine Capture in Silver-Containing Mordenites through Nanoscale Silver Iodide Formation. *J. Am. Chem. Soc.* **2010**, *132*, 8897−8899.

(12) Garino, T. J.; Nenoff, T. M.; Krumhansl, J. L.; Rademacher, D. X. Low-Temperature Sintering Bi−Si−Zn-Oxide Glasses for Use in Either Glass Composite Materials or Core/Shell ^{129}I Waste Forms. *J. Am. Ceram. Soc.* **2011**, *94*, 2412−2419.

(13) Maddrell, E. R.; Vance, E. R.; Gregg, D. J. Capture of Iodine from the Vapour Phase and Immobilisation as Sodalite. *J. Nucl. Mater.* **2015**, *467*, 271−279.

(14) Bruffey, S. H.; Jubin, R. T.; Jordan, J. A. Capture of Elemental and Organic Iodine from Dilute Gas Streams by Silver-Exchanged Mordenite. *Procedia Chem.* **2016**, *21*, 293−299.

(15) Sava, D. F.; Garino, T. J.; Nenoff, T. M. Iodine Confinement into Metal-Organic Frameworks (MOFs): Low-Temperature Sintering Glasses to Form Novel Glass Composite Material (GCM) Alternative Waste Forms. *Ind. Eng. Chem. Res.* **2012**, *51*, 614−620.

(16) Banerjee, D.; Chen, X.; Lobanov, S. S.; Plonka, A. M.; Chan, X.; Daly, J. A.; Kim, T.; Thallapally, P. K.; Parise, J. B. Iodine Adsorption in Metal Organic Frameworks in the Presence of Humidity. *ACS Appl. Mater. Interfaces* **2018**, *10*, 10622−10626.

(17) Matyáš, J.; Ilton, E. S.; Kovařík, L. Silver-Functionalized Silica Aerogel: Towards an Understanding of Aging on Iodine Sorption Performance. *RSC Adv.* **2018**, *8*, 31843−31852.
(18) Riley, B. J.; Chong, S.; Olszta, M. J.; Peterson, J. A. Evaluation of Getter Metals in Na-Al-Si-O Aerogels and Xerogels for the Capture of Iodine Gas. *ACS Appl. Mater. Interfaces* **2020**, *12*, 19682−19692.
(19) Fukasawa, T.; Funabashi, K.; Kondo, Y. Influences of Impurities on Iodine Removal Efficiency of Silver Alumina Adsorbent. In*24th DOE/NRC Nuclear Air Cleaning and Treatment Conference*; NUREG-CP-0153, 1996; Vol. *29*.
(20) Metalidi, M. M.; Beznosyuk, V. I.; Kalinin, N. N.; Kolyadin, A. B.; Fedorov, Y. S. Treatment of Gas-Air Flows to Remove Radioiodine Using Metallic Copper. *Radiochem* **2009**, *51*, 409−411.
(21) Beck, C. L.; Riley, B. J.; Chong, S.; Smith, N.; Seiner, D. R.; Seiner, B. N.; Engelhard, M. H.; Clark, S. B. Molecular Iodine Interactions with Fe, Ni, Cr, and Stainless Steel Alloys. *Ind. Eng. Chem. Res.* **2021**, *60*, 2447−2454.
(22) Matyáš, J.; Fryxell, G. E.; Busche, B. J.; Wallace, K.; Fifield, L. S. Functionalized Silica Aerogels: Advanced Materials to Capture and Immobilize Radioactive Iodine. *Ceramics Engineering and Science Proceedings*; Lin, H.-T., Katoh, Y., Fox, K. M., Belharouak, I., Widjaja, S., Singh, D., Eds.; Wiley-The American Ceramic Society: Daytona Beach, FL, 2011; Vol. *32*, pp 23−33.
(23) Riley, B. J.; Kroll, J. O.; Peterson, J. A.; Matyáš, J.; Olszta, M. J.; Li, X.; Vienna, J. D. Silver-Loaded Aluminosilicate Aerogels as Iodine Sorbents. *ACS Appl. Mater. Interfaces* **2017**, *9*, 32907−32919.
(24) Tesfay Reda, A.; Pan, M.; Zhang, D.; Xu, X. Bismuth-Based Materials for Iodine Capture and Storage: A Review. *J. Environ. Chem. Eng.* **2021**, *9*, 105279.
(25) Cordova, E. A.; Garayburu-Caruso, V.; Pearce, C. I.; Cantrell, K. J.; Morad, J. W.; Gillispie, E. C.; Riley, B. J.; Colon, F. C.; Levitskaia, T. G.; Saslow, S. A.; Qafoku, O.; Resch, C. T.; Rigali, M. J.; Szecsody, J. E.; Heald, S. M.; Balasubramanian, M.; Meyers, P.; Freedman, V. L. Hybrid Sorbents for ^{129}I Capture from Contaminated Groundwater. *ACS Appl. Mater. Interfaces* **2020**, *12*, 26113−26126.
(26) Tesfay Reda, A.; Zhang, D.; Xu, X.; Pan, M.; Chang, C.; Muhire, C.; Liu, X.; Jiayi, S. Bismuth-Impregnated Aluminum/Copper Oxide-Pillared Montmorillonite for Efficient Vapor Iodine Sorption. *Sep. Purif. Technol.* **2021**, *270*, 118848.
(27) Thomas, T. R.; Murphy, L. P.; Staples, B. A.; Nichols, J. T. Airborne Elemental Iodine Loading Capacities of Metal Zeolites and a Method for Recycling Silver Zeolite. *ICP-1119*; Idaho National Laboratory: Idaho Falls, ID, 1977.
(28) Riley, B. J.; Pierce, D. A.; Chun, J.; Matyáš, J.; Lepry, W. C.; Garn, T. G.; Law, J. D.; Kanatzidis, M. G. Polyacrylonitrile-Chalcogel Hybrid Sorbents for Radioiodine Capture. *Environ. Sci. Technol.* **2014**, *48*, 5832−5839.
(29) Cao, C.; Chong, S.; Thirion, L.; Mauro, J. C.; McCloy, J. S.; Goel, A. Wet Chemical Synthesis of Apatite-Based Waste Forms—A Novel Room Temperature Method for the Immobilization of Radioactive Iodine. *J. Mater. Chem. A* **2017**, *5*, 14331−14342.
(30) Chong, S.; Peterson, J. A.; Riley, B. J.; Tabada, D.; Wall, D.; Corkhill, C. L.; McCloy, J. S. Glass-Bonded Iodosodalite Waste Form for Immobilization of ^{129}I. *J. Nucl. Mater.* **2018**, *504*, 109−121.
(31) Chong, S.; Riley, B. J.; Asmussen, R. M.; Lawter, A. R.; Bruffey, S. H.; Nam, J.; McCloy, J. S.; Crum, J. V. Iodosodalite Synthesis with Hot Isostatic Pressing of Precursors Produced from Aqueous and Hydrothermal Processes. *J. Nucl. Mater.* **2020**, *538*, 152222.
(32) Riley, B. J.; Chong, S.; Beck, C. L. Iodine Vapor Reactions with Pure Metal Wires at Temperatures of 100-139 °C in Air. *Ind. Eng. Chem. Res.* **2021**, *60*, 17162−17173.
(33) *Environmental Protection Agency 40 CFR 261*; Environmental Protection Agency: Washington, D.C., 2012.
(34) Matyáš, J.; Sannoh, S. E.; Li, X. S. *Development of a Robust Ag^0-Functionalized Silica Aerogel for Capturing Iodine Gas, PNNL-30732*; Pacific Northwest National Laboratory: Richland, WA, 2020.
(35) Hersh, C. K. *Molecular Sieves*; Reinhold Publishing Company: New York, NY, 1961.
(36) Maeck, W. J.; Pence, D. T.; Keller, J. H. *A Highly Efficient Inorganic Adsorber for Airborne Iodine Species (Silver Zeolite Development Studies), IN-1224*; Idaho Nuclear Corporation - National Reactor Testing Station: Idaho Falls, ID, 1968.
(37) Julbe, A.; Drobek, M. Zeolite X: Type. In *Encyclopedia of Membranes*; Drioli, E., Giorno, L., Eds.; Springer Berlin Heidelberg: Berlin, Heidelberg, 2015; pp 1−2.
(38) Lutz, W. Zeolite Y: Synthesis, Modification, and Properties-A Case Revisited. *Adv. Mater. Sci. Eng.* **2014**, *2014*, 724248.
(39) Riley, B. J.; Chong, S.; Schmid, J.; Marcial, J.; Nienhuis, E. T.; Bera, M. K.; Lee, S.; Canfield, N. L.; Kim, S.; Derewinski, M. A.; Motkuri, R. K. Role of Zeolite Structural Properties toward Iodine Capture: A Head-to-head Evaluation of Framework Type and Chemical Composition. *ACS Appl. Mater. Interfaces* **2022**, *14*, 18439−18452.
(40) Gattu, V. K.; Stariha, S.; Lee, E.; Fortner, J. A.; Ebert, W. L. *Degradation Tests with Iodide Waste Forms: FY20 Status Report. ANL/CFCT-20/22*; Argonne National Laboratory: Lemont, IL, 2020.
(41) Reiser, J. T.; Lawter, A. R.; Avalos, N. A.; Bonnett, J.; Riley, B. J.; Chong, S.; Canfield, N.; Saslow, S. A.; Bourchy, A.; Asmussen, R. M. Review and Experimental Comparison of the Durability of Iodine Waste Forms in Semi-Dynamic Leach Testing. *Chem. Eng. J. Adv.* **2022**, *11*, 100300.
(42) Linde, D. R. *CRC Handbook of Chemistry and Physics*; 88th ed.; CRC Press: Boca Raton, FL, 2007.
(43) Abney, C. W.; Nan, Y.; Tavlarides, L. L. X-ray Absorption Spectroscopy Investigation of Iodine Capture by Silver-Exchanged Mordenite. *Ind. Eng. Chem. Res.* **2017**, *56*, 4837−4846.
(44) Cicconi, M. R.; Pili, E.; Grousset, L.; Florian, P.; Bouillard, J. C.; Vantelon, D.; Neuville, D. R. Iodine Solubility and Speciation in Glasses. *Sci. Rep.* **2019**, *9*, 7758.
(45) Ferraria, A. M.; Carapeto, A. P.; Botelho do Rego, A. M. X-Ray Photoelectron Spectroscopy: Silver Salts Revisited. *Vacuum* **2012**, *86*, 1988−1991.
(46) Cheary, R. W.; Coelho, A. A.; Cline, J. P. Fundamental Parameters Line Profile Fitting in Laboratory Diffractometers. *J. Res. Natl. Inst. Stand. Technol.* **2004**, *109*, 1−25.
(47) Toby, B. H. 4.2. Powder dictionary (pdCIF). In *International Tables for Crystallography Volume G: Definition and Exchange of Crystallographic Data*; Hall, S. R., McMahon, B., Eds.; International Union of Crystallography, 2006; pp 258−269. DOI: 10.1107/9780955360206000742
(48) Brunauer, S.; Emmett, P. H.; Teller, E. Adsorption of Gases in Multimolecular Layers. *J. Am. Chem. Soc.* **1938**, *60*, 309−319.
(49) Gregg, S.; Sing, K. *Adsorption, Surface Area, and Porosity*, 2nd ed.; Academic Press: Orlando, 1982.
(50) Chong, S.; Riley, B. J.; Kuang, W.; Olszta, M. J. Iodine Capture with Mechanically Robust Heat-Treated Ag-Al-Si-O Xerogel Sorbents. *ACS Omega* **2021**, *6*, 11628−11638.
(51) Chong, S.; Riley, B. J.; Peterson, J. A.; Olszta, M. J.; Nelson, Z. J. Gaseous Iodine Sorbents: A Comparison Between Ag-Loaded Aerogel and Xerogel Scaffolds. *ACS Appl. Mater. Interfaces* **2020**, *12*, 26127−26136.
(52) Lopez-Salido, I.; Lim, D. C.; Kim, Y. D. Ag Nanoparticles on Highly Ordered Pyrolytic Graphite (HOPG) Surfaces Studied Using STM and XPS. *Surf. Sci.* **2005**, *588*, 6−18.
(53) Yoshiasa, A.; Koto, K.; Kanamaru, F.; Emura, S.; Horiuchi, H. Anharmonic Thermal Vibrations in Wurtzite-Type AgI. *Acta Crystallogr., Sect. B: Struct. Sci.* **1987**, *43*, 434−440.
(54) Adams, L. H.; Davis, B. L. Rapidly Running Transitions at High Pressure. *Proc. Natl. Acad. Sci.* **1962**, *48*, 983−990.
(55) Firet, N. J.; Blommaert, M. A.; Burdyny, T.; Venugopal, A.; Bohra, D.; Longo, A.; Smith, W. A. Operando EXAFS Study Reveals Presence of Oxygen in Oxide-Derived Silver Catalysts for Electrochemical CO_2 Reduction. *J. Mater. Chem. A* **2019**, *7*, 2597−2607.
(56) Matyáš, J. *Silver-Functionalized Silica Aerogel for Testing at ORNL, FCRD-MRWD-2015-000697*; Pacific Northwest National Laboratory: Richland, WA, 2014.

(57) Matyáš, J. *Silver-Functionalized Silica Aerogel for Testing at INL, FCRD-MRWD-2015-00698*; Pacific Northwest National Laboratory: Richland, WA, 2015.
(58) Matyáš, J. *Silver-Functionalized Silica Aerogel for FY18 Testing at INL, PNNL-27245, NTRD-MRWFD-2018-000219*; Pacific Northwest National Laboratory: Richland, WA, 2018.
(59) Matyáš, J. *Silver-Functionalized Silica Aerogel for FY19 Testing at ORNL, PNNL-28410*; Pacific Northwest National Laboratory: Richland, WA, 2019.
(60) Strachan, D. M.; Chun, J.; Matyas, J.; Lepry, W.; Riley, B. J.; Ryan, J. V.; Thallapally, P. K. *Summary Report on the Volatile Radionuclide and Immobilization Research for FY2011 at PNNL, FCRD-SWF-2011-000378, PNNL-20807*; Pacific Northwest National Laboratory: Richland, WA, 2011.
(61) Tian, Z.; Chee, T.-S.; Zhu, L.; Duan, T.; Zhang, X.; Lei, L.; Xiao, C. Comprehensive Comparison of Bismuth and Silver Functionalized Nickel Foam Composites in Capturing Radioactive Gaseous Iodine. *J. Hazard. Mater.* **2021**, *417*, 125978.
(62) Matyas, J.; Ilton, E. S.; Lahiri, N.; Li, X. S.; Silverstein, J. A. *Bismuth-Functionalized Silica Aerogels for Iodine Capture, PNNL-32086*; Pacific Northwest National Laboratory: Richland, WA, 2021.
(63) Tian, Z.; Chee, T.-S.; Zhang, X.; Lei, L.; Xiao, C. Novel Bismuth-Based Electrospinning Materials for Highly Efficient Capture of Radioiodine. *Chem. Eng. J.* **2021**, *412*, 128687.
(64) Donnay, J. D. H.; Ondik, H. M. *Crystal Data Determinative Tables*, 3rd ed.; US Department of Commerce: Swarthmore, PA, 1973; Vol. *4*.
(65) Yang, J. H.; Shin, J. M.; Park, J. J.; Park, G. I.; Yim, M. S. Novel Synthesis of Bismuth-Based Adsorbents for the Removal of ^{129}I in Off-Gas. *J. Nucl. Mater.* **2015**, *457*, 1−8.
(66) Sava, D. F.; Chapman, K. W.; Rodriguez, M. A.; Greathouse, J. A.; Crozier, P. S.; Zhao, H.; Chupas, P. J.; Nenoff, T. M. Competitive I_2 Sorption by Cu-BTC from Humid Gas Streams. *J. Am. Chem. Soc.* **2013**, *25*, 2591−2596.
(67) Subrahmanyam, K. S.; Sarma, D.; Malliakas, C. D.; Polychronopoulou, K.; Riley, B. J.; Pierce, D. A.; Chun, J.; Kanatzidis, M. G. Chalcogenide Aerogels as Sorbents for Radioactive Iodine. *Chem. Mater.* **2015**, *27*, 2619−2626.
(68) Qian, X.; Wang, B.; Zhu, Z.-Q.; Sun, H.-X.; Ren, F.; Mu, P.; Ma, C.; Liang, W.-D.; Li, A. Novel N-Rich Porous Organic Polymers with Extremely High Uptake for Capture and Reversible Storage of Volatile Iodine. *J. Hazard. Mater.* **2017**, *338*, 224−232.
(69) Wang, P.; Xu, Q.; Li, Z.; Jiang, W.; Jiang, Q.; Jiang, D. Exceptional Iodine Capture in 2D Covalent Organic Frameworks. *Adv. Mater.* **2018**, *30*, 1801991.
(70) Xie, W.; Cui, D.; Zhang, S.-R.; Xu, Y.-H.; Jiang, D.-L. Iodine Capture in Porous Organic Polymers and Metal-Organic Frameworks Materials. *Mater. Horiz.* **2019**, *6*, 1571−1595.

https://doi.org/10.1021/acsanm.2c01741
ACS Appl. Nano Mater. 2022, 5, 9478−9494